

NASA TECHNICAL NOTE



NASA TN D-4245

8.1

NASA TN D-4245

LOAN COPY: RETURN
AFWL (WLL-2)
HURLAND AFB, NM

0130840



TECH LIBRARY KAFB, NM

FREE-FLIGHT AERODYNAMIC
CHARACTERISTICS OF A SLENDER CONE
BETWEEN MACH NUMBERS OF 7 AND 8

by Joseph H. Judd

Langley Research Center

Langley Station, Hampton, Va.





0130840

NASA TN D-4245

FREE-FLIGHT AERODYNAMIC CHARACTERISTICS OF A SLENDER CONE
BETWEEN MACH NUMBERS OF 7 AND 8

By Joseph H. Judd

Langley Research Center
Langley Station, Hampton, Va.

NATIONAL AERONAUTICS AND SPACE ADMINISTRATION

For sale by the Clearinghouse for Federal Scientific and Technical Information
Springfield, Virginia 22151 - CFSTI price \$3.00

FREE-FLIGHT AERODYNAMIC CHARACTERISTICS OF A SLENDER CONE BETWEEN MACH NUMBERS OF 7 AND 8

By Joseph H. Judd
Langley Research Center

SUMMARY

A free-flight test of a 3.56° half-angle cone configuration was made by use of the rocket test technique. The cone model was accelerated to a Mach number of 8 and a Reynolds number based on nominal body length of 25×10^6 . Data are presented during the decelerating flight to a Mach number of 7 and a Reynolds number based on body length of 2.5×10^6 as the slowly spinning cone was disturbed in pitch by pulse rockets.

The cone model demonstrated a good aerodynamic efficiency, having a lift-drag ratio of 2.77 at a Mach number of 7.3 and at an angle of incidence of 9° . During the decelerating flight a relatively steady value of the roll resonance parameter, approximately 0.8, was maintained. The measured variation of axial-force coefficient with resultant-force coefficient in the transverse plane agreed with estimated values obtained by using Newtonian theory and classical hypersonic similarity, although the estimated values obtained by using similarity were slightly lower.

INTRODUCTION

The use of lift during the atmospheric portion of high-speed flight can extend the range and change the direction of flight of aerospace vehicles. The development of efficient aerodynamic configurations promises an increase in operational flexibility for reentry vehicles and tends to make hypersonic boost-glide craft competitive with lower speed aircraft. Studies of such configurations form, therefore, a part of the research effort of the Langley Research Center. A representative group of slender-body and wing-body configurations is described in reference 1 which presents results of an investigation conducted in the Langley 4- by 4-foot supersonic pressure tunnel at Mach numbers of 1.41 and 2.01. Flight tests of several of these configurations were made to measure static and dynamic aerodynamic coefficients and derivatives at transonic and high supersonic speeds (see, for example, refs. 2 and 3). A further goal of this research effort was the correlation between data obtained from wind-tunnel tests, free-flight tests, and various methods of computation. The present paper reports the results of a flight test — that of a slender cone of fineness ratio 8.

The cone flight test, made by using the rocket test technique, was conducted at Wallops Station. The data were obtained during decelerating flight and are presented from a Mach number of 8 and a Reynolds number based on body length of 25×10^6 to a Mach number 7 and a Reynolds number based on body length of 2.5×10^6 .

SYMBOLS

The relations between the axis systems, velocities, accelerations, and force coefficients used in this report are shown in figure 1. Measurements and data were taken in the U.S. Customary System of Units. Equivalent values are given parenthetically in the International System (SI).

$$A_N = -A_Z$$

A_X, A_Y, A_Z linear acceleration along X-, Y-, and Z-axis, respectively (see fig. 1(a)),
g units

C_A axial-force coefficient (including base drag)

C_D drag coefficient

$C_{D,b}$ base-drag coefficient

C_L lift coefficient

C_m pitching-moment coefficient

C_N normal-force coefficient

C_n yawing-moment coefficient

$C_{p,b}$ base-pressure coefficient

C_R resultant-force coefficient in transverse plane

C_Y side-force coefficient

d diameter of cone base, feet (meters)

I_X, I_Y, I_Z	mass moment of inertia about X-, Y-, and Z-axis, respectively, slug-foot ² (kilogram-meter ²)
K	hypersonic similarity parameter
l	nominal body length, feet (meters)
M_∞	free-stream Mach number
p, q, r	roll, pitch, and yaw velocity, respectively, radians/second
q_∞	free-stream dynamic pressure, pounds force/foot ² (newtons/meter ²)
R	Reynolds number based on nominal body length
S	area of cone base (reference area), foot ² (meter ²)
t	time, seconds
u, v, w	relative velocity components in body-axis system, feet/second (meters/second)
V_∞	free-stream velocity, feet/second (meters/second)
W	weight, pounds force (newtons)
X, Y, Z	body-axis system located at center of gravity
x, y, z	body-axis-system ordinates
x_{cg}	location of center of gravity measured from reference station 0 (see fig. 2), positive rearward, feet (meters)
x_{cp}	location of center of pressure measured from reference station 0, positive rearward, feet (meters)
X_g, Y_g, Z_g	gravity-axis system
α	angle of attack, degrees

β	angle of sideslip, degrees
γ	mean flight-path angle in vertical plane of gravity-axis system, degrees
η	angle between free-stream velocity vector and X-axis (angle of incidence), degrees
θ, ψ, φ	pitch, yaw, and roll Euler attitude angles referred to gravity-axis system, degrees
τ	fineness ratio, l/d
$\Delta\omega/\omega_0$	roll resonance parameter (as defined in ref. 6)

A dot over a symbol denotes the derivative with respect to time.

MODELS AND APPARATUS

Flight-Test Model

The flight-test configuration was a slender cone of nominal fineness ratio 8. A drawing and photographs of the model are given in figures 2 and 3, and the physical properties are listed in table I. The cone apex was blunted by using a 0.375-inch-radius (0.0095-meter-radius) spherical element to delay nose melting or burning beyond the data-gathering portion of the flight. In order to match the telemeter impedance in free flight to that on the rocket vehicle, a bell-shaped aluminum ring was mounted on the rearmost former and extended 0.250 inch (0.00635 meter) behind the base of the cone (see fig. 3(b)).

The nose of the cone was machined from a solid steel block. All internal structure, including the telemeter deck, was steel; the outer skin was stainless steel. The telemeter deck, including instrument mounts, was located in the forward section of the model and was covered by a truncated-cone thermal-radiation shield of aluminum. The cone surface was smooth and unbroken with the exception of three pulse-rocket nozzle openings and small slots for the prongs of an external power plug. The skin was slotted at the base along a conic element for the telemeter antenna, but the slot was filled with a piece of ceramic which was faired to the cone surface. The base of the cone was open, on the outside of the bell-shaped ring, to the rearmost former and, on the inside of the bell-shaped ring, to a rear bulkhead located approximately 2 feet (0.61 meter) forward of the cone base. A 0.250-inch (0.00635-meter) rim was used around the cone base.

Three pulse rockets whose cases were machined in the nose block were used. The exhaust-nozzle center lines were located in the XZ-plane and are shown in figure 2.

The weight, center-of-gravity location, and mass moments of inertia of the model are given in table I. Structural design symmetry and internal component location were used to provide mass symmetry about the cone center line. Insofar as could be measured by using the pendulum technique, the principal axis of the model lay along the geometric center line. However, the spin-table technique was not used to either statically or dynamically balance the model.

Launch Vehicle

The launch vehicle consisted of the model and three stages of rocket propulsion. A photograph of the assembled vehicle mounted on the launcher is shown in figure 4. Propulsion elements were an Honest John rocket motor for the first stage, a Nike-booster rocket motor for the second stage, and a Gosling rocket motor for the third stage. The first and second stages were fin stabilized, whereas the third stage was flare stabilized.

Instrumentation

Model.- Six linear accelerometers were mounted inside the model. Locations of the sensing elements, measured from the model center of gravity, are listed in table II. The acceleration range of the transverse and normal accelerometers was selected to cover the accelerations expected during disturbances produced by the pulse rockets. However, the high-range longitudinal accelerometer was calibrated to measure accelerations occurring during rocket motor firing and the low-range longitudinal accelerometer was calibrated to measure decelerations of coasting flight. Two rate gyros were installed to measure the angular velocity in pitch and roll. Pressure was measured at the nose of the model through an orifice on the cone center line, and base pressure was measured by a pressure gage connected to the cavity between the model outer skin and the aluminum bell-shaped ring. Measurements from these instruments were transmitted to ground receiving stations by a National Aeronautics and Space Administration 10-channel FM/AM telemeter.

Range instruments.- Ground-based instruments used during the flight test consisted of tracking cameras, tracking radar, and telemeter receiving stations. Three radar sets were used to measure the position of the model - an SCR-584 S-band radar modified by NASA for missile tracking, a Reeves Mod. II SCR-584 radar, and an RCA AN/FPS-16 C-band radar. Three ground receiving telemeter stations were located at Wallops Station and, in addition, the Wallops sea-range telemeter trailer was onboard a Navy ship about 70 international nautical miles (130 km) downrange from the launch site and slightly south of the model ground track.

TESTS

The flight vehicle was launched from Wallops Station at a nominal elevation angle of 75° and azimuth angle of 125° . The time t used in this report was measured from the application of the electrical firing current to the first-stage rocket motor. Following burnout of the third-stage rocket motor, the relative deceleration between the model and the third stage caused a smooth separation at 63.5 seconds. Pulse rockets, ignited at 65.1, 68.3, and 76.4 seconds, applied a force in the XZ-plane near the nose of the cone. The aerodynamic and motion data presented herein were obtained during the decelerating flight of the model after separation.

Although all the position radars tracked the rocket vehicle and model, the data used in the measurement analysis were obtained solely from the FPS-16 radar. The model altitude obtained from analysis of the trajectory was corrected for the curvature of the earth. Model inertial velocity was obtained by differentiation of distance along the flight path with respect to time. Atmospheric environment data were provided by a radiosonde-carrying balloon whose position was tracked by radar. Wind velocity was obtained by analysis of the balloon flight path and was vectorially added to the inertial velocity of the model to give the velocity of the model through the air. Velocity and Mach number data are presented in figure 5.

Atmospheric density and temperature were measured by the radiosonde to the peak balloon altitude of about 85 000 feet (25 900 meters). Then these measured data were extrapolated to cover the data portion of the flight, about 105 000 feet (32 000 meters), by fairing to the standard altitude properties as given in reference 4. The variation of the dynamic pressure with time is shown in figure 5, and the variation of Reynolds number based on body length with Mach number is shown in figure 6.

ANALYSIS OF FLIGHT DATA

The coplanar accelerometers allow the calculation of the total linear acceleration at any desired point along the model axis by use of the relationships given in reference 5. However, all the accelerometer data used in the present analysis were obtained at the model center of gravity. The total force coefficients were obtained by multiplying these accelerations by $W/q_\infty S$.

Since the cone model is symmetrical, the normal- and side-force coefficients can be added vectorially to form a resultant-force coefficient which is a function of the angle η between the X-axis and the wind vector. Figure 1(c) shows the relationships between the coefficients. The variation of measured coefficients with time is presented in figure 7.

Algebraic manipulation of the equations for planar accelerations allows the quantities $\dot{q} - rp$ and $\dot{r} + qp$ to be determined from coplanar-accelerometer data. However, the pitch rate gyro failed in flight and the pitching and yawing velocities could not be computed. For this reason, the moments were approximated by neglecting I_X , as shown in the following equations:

$$\text{Pitching moment} = I_Y \dot{q} - (I_Z - I_X)rp \approx I_Y(\dot{q} - rp)$$

$$\text{Yawing moment} = I_Z \dot{r} + (I_Y - I_X)qp \approx I_Z(\dot{r} + qp)$$

Neglecting I_X introduces an error equal to or less than 2.4 percent in the pitching and yawing moments. It is possible to make the approximation since the moments of inertia I_Z and I_Y are equal. The total moment coefficients C_m and C_n are obtained by dividing the corresponding moments by $q_\infty S d$. Time histories of these coefficients are presented in figures 7(f) and 7(g).

Calculations were made to determine the errors involved in the data. The probable instrument error was 1 percent of the full-scale range. The computed errors, based on this value, are given in the following table:

Time, sec	Error in -				
	C_A	C_N and C_Y	C_m	C_n	$C_{D,b}$
64.0	0.003	0.024	0.058	0.057	0.009
68.0	.005	.043	.099	.096	.017
72.0	.008	.068	----	----	----

Preliminary plans for obtaining the aerodynamic derivatives from the measured flight motions provided for the application of the methods of reference 5 if the model did not roll in flight, and for the procedures outlined in reference 6 if roll was encountered during the flight test. As the data presented in figure 8 show, the cone was rolling after separation from the final boost stage. Cross plots of the force coefficients C_N and C_Y were made (see fig. 9), and the external and internal envelopes enclosing the points were drawn as illustrated in figure 1(c). The trim center was estimated to fall at the radius of curvature of these envelopes. With the use of the estimated trim center, the roll resonance parameter $\Delta\omega/\omega_0$ was computed by using the angles between successive maximum values of C_R and the times at which these peaks occurred as shown in reference 6. These data are presented in figure 10. Values of $C_{R,\text{maximum}} - C_{R,\text{minimum}}$ were measured between the inner and outer envelopes, the data points being taken where the trace of the data was tangent to the envelope. The data plotted in figure 11 show that

a pronounced variation in the oscillation amplitude exists with time. This makes the computation of aerodynamic derivatives by the techniques of reference 6 of little or no value. Indeed, a close examination of the data of a sample case in the reference indicated a similar but much smaller variation.

RESULTS AND DISCUSSION

Aerodynamic Coefficients

The variation of the normal-force, side-force, and axial-force coefficients with time is shown in figures 7(a), 7(b), and 7(c), respectively. Figure 12 presents the variation of axial-force coefficient with resultant-force coefficient at several Mach numbers. It should be noted that the data are presented over a complete cycle of oscillation for each Mach number and that the increment in Mach number is 0.03. Two estimates of the cone aerodynamic coefficients (hypersonic similarity and Newtonian impact theory) are also shown in the figure. Both estimates were obtained by summing the spherical-nose drag, the base drag, and the cone-surface drag. For the dashed curve the cone-surface force coefficients were obtained by using measured wind-tunnel data (including friction effects) which were transformed to values for a cone of fineness ratio 8 by using the classical hypersonic similarity parameters. The methods used to accomplish this transformation are explained in appendix A. The shaded region on the graph represents inviscid Newtonian impact theory, with the lower limit having an additional increment of drag due to skin friction of a laminar boundary layer and with the upper limit having an increment due to skin friction of a completely turbulent boundary layer; both skin-friction drag increments were estimated at the corresponding Mach number and Reynolds number by using the methods of references 7 and 8. All the experimental data of figure 12 fell within the limits estimated by using the Newtonian theory pressure drag to which was added a viscous contribution. Estimates of axial-force coefficient obtained by using the experimental drag measured in wind-tunnel tests, including the effects of friction drag, were generally lower than the values measured in the flight test, but showed good correlation. The indication is that hypersonic similarity laws can be used to transform measured total-drag data to values for slenderer affine bodies at higher Mach numbers; this result is particularly significant for bodies at angles of incidence. It appears that since the classical hypersonic similarity theory predicted only the trend, consideration of the viscous similarity parameters, as outlined in reference 9, may improve the correlation.

The lift-drag ratio was computed by using data in figure 12 and the estimated variation of resultant-force coefficient with angle of incidence in figure 13(b). The maximum value of lift-drag ratio was 2.77 at a Mach number of 7.3 and an angle of incidence of 9° .

Measured base-pressure coefficients are shown in figure 7(e) by data points, and the estimated coefficients at zero angle of incidence from reference 10 are indicated by a dashed line. In order to determine the effect of angle of incidence, the base-drag coefficient (which is numerically equal to $C_{p,b}$) was plotted as a function of resultant-force coefficient at a free-stream Mach number of 7.8 (see fig. 14). For the range of resultant-force coefficient shown, no significant trend is evident.

The pitching-moment and yawing-moment coefficients from figure 7(g) are plotted as functions of normal-force and side-force coefficients, respectively, in figure 15 for several cycles of oscillation. The moment about the center of gravity due to the normal-force coefficient acting at $\frac{2}{3}l$ is also shown in this figure. The average slope of the data agrees with the estimation, indicated by the dashed line. However, a certain amount of hysteresis is evident in the data as well as an apparent trim moment coefficient at zero force coefficients. This trim moment coefficient could be caused by a small mass unbalance or a slight bending of the model due to aerodynamic heating, pulse rocket firing, or combinations of these factors and may be amplified by the roll of the model.

Model Motion Description

The flight model separated from the third-stage booster with a rolling velocity of nearly 10 radians per second. Firing of the first pulse rocket of 65.1 seconds produced an appreciable disturbance in pitch, as shown in figure 7(a). The roll resonance parameter for this combination of pitching and rolling velocity (fig. 10) was initially $\Delta\omega/\omega_0 = 0.68$. When, however, the natural frequency in pitch decreased because of the decrease in dynamic pressure, the roll resonance parameter increased to approximately 0.8 and then remained nearly constant. The relatively steady value of the roll resonance parameter was due to a decrease in the rate of roll.

The model motion corresponds to a phenomenon called "roll lock-in," which is described in references 11 and 12. These analytical studies showed that when a spinning configuration had a nonzero pitching moment, a zero resultant-force coefficient, and a small displacement of the center of gravity from the center line, the motions tended to stabilize at a fixed ratio of rolling velocity to pitching frequency, even for some impressed value of rolling moment.

Measured aerodynamic data for the cone (fig. 15) indicate a positive pitching moment at zero resultant force. Since the model was not dynamically balanced, it was possible that (1) the center of gravity was slightly displaced from the geometric cone axis, or (2) the products of inertia were not zero. A review of figure 9 suggests that the motions of the cone were characteristic of roll lock-in.

Reference 12, in which linear aerodynamic theory was used, describes the criteria of oscillatory roll resonance, whereby the roll rate of a vehicle with an offset center of

gravity and no roll damping tends to oscillate at two modes, a high-frequency mode with small amplitude and a low-frequency mode with larger amplitude. The rolling-velocity data (fig. 8) show one such oscillatory frequency superimposed on a decreasing roll rate. By using the average flight conditions at the first cycle and average slopes of the aerodynamic coefficients and derivatives, the period of the low-frequency oscillation was calculated to be 3.49 seconds and the period of the high-frequency oscillation, 0.581 second.

CONCLUDING REMARKS

A slender cone configuration of nominal fineness ratio 8 was accelerated by a multi-stage rocket vehicle to a Mach number of 8 and a Reynolds number based on the nominal body length of 25×10^6 . Data obtained during the decelerating flight after separation of the model from the final stage of the boost vehicle were analyzed. A comparison between the measured variation of axial-force coefficient with resultant-force coefficient and the variation estimated by using the sum of Newtonian pressure forces and average skin-friction coefficients showed excellent correlation. Another estimate obtained by using measured data from wind-tunnel tests on conical models of lower fineness ratio, which were transformed to values for a cone of fineness ratio 8 by using the classical hypersonic similarity parameters, showed values of axial-force coefficient slightly lower than the flight-test values. During the flight test the cone maintained a relatively steady value of the roll resonance parameter near resonance, and some evidence of roll lock-in was obtained from analysis of the model motion.

Langley Research Center,
National Aeronautics and Space Administration,
Langley Station, Hampton, Va., June 15, 1967,
124-07-02-16-23.

APPENDIX A

PROCEDURES FOR ESTIMATING CONE AERODYNAMIC COEFFICIENTS

The estimated aerodynamic coefficients for the cone with a fineness ratio of 8 are required for comparison with the aerodynamic coefficients that were measured in the flight test. An explanation of the methods used to obtain such estimated values is given in the following paragraphs, with emphasis on the transformation of the experimental data by the hypersonic similarity parameters.

The three factors which contribute to the forces acting on the cone are (1) the pressures on the cone surface, (2) the pressure on the cone base, and (3) the friction acting on the surface. At zero angle of incidence, the pressures on the cone surface, including the effect of the boundary layer, may be computed with good accuracy. However, with the cone inclined at an angle of incidence to the flow, the nature of the boundary layer and its effect on the surface pressures become difficult to calculate. This difficulty results from two major uncertainties – the variation of the displacement thickness around the circumference of the cone and the location of the transition from laminar flow to turbulent flow in the boundary layer.

In order to circumvent the uncertainties associated with the flow over the cone surface, an attempt was made to use measured cone aerodynamic data. The basic procedure involved taking measured data for a cone of an arbitrary included angle and various angles of incidence and transforming these data to values for a cone with fineness ratio 8 at an equivalent Mach number. At high Mach numbers the hypersonic similarity parameter is $K = \gamma M_\infty$, but for the Mach numbers in the present investigation, reference 13 indicates that the relationship $K = \gamma \sqrt{M_\infty^2 - 1}$ is valid.

Measured wind-tunnel data are usually reported in the form of the variation of C_L and C_D at constant test conditions M_∞ and R with angle of incidence. The computation procedure used herein involved calculating K by using the test Mach number and fineness ratio. From the calculated value of K and the value of τ for a cone with fineness ratio 8, a Mach number at which the transformed data would be applicable was computed. The equations which yield the transformed data are as follows:

$$(\eta)_{\text{transformed}} = \frac{(\sqrt{M_\infty^2 - 1} \eta)_{\text{measured}}}{(\sqrt{M_\infty^2 - 1})_{\text{transformed}}}$$

APPENDIX A

$$(C_L)_{\text{transformed}} = \frac{(\sqrt{M_\infty^2 - 1} C_L)_{\text{measured}}}{(\sqrt{M_\infty^2 - 1})_{\text{transformed}}}$$

$$(C_D)_{\text{transformed}} = \frac{[(M_\infty^2 - 1) C_D]_{\text{measured}}}{(M_\infty^2 - 1)_{\text{transformed}}}$$

The transformed data are then referred to the body-axis system, and the variations of C_A and C_R with η are obtained and plotted. Next, values of these coefficients are taken from the curves at several desired angles of incidence, 0° , 2° , 4° , 6° , 8° , 10° , and 12° , and plotted on a graph of force coefficient as a function of Mach number.

Experimental data were taken from references 14, 15, 16, and 17, transformed according to the aforementioned procedure, and plotted. Curves faired through these points gave the cone-surface force coefficients as functions of Mach number for the angle-of-incidence range of interest.

The effect of the spherical nose as a contribution to the axial-force coefficient was checked and found to be a substantial increment. Therefore, an increment due to the front part of a sphere was estimated and added to the forebody axial-force coefficient. The total forebody axial-force coefficients and resultant-force coefficients thus obtained are plotted in figure 13.

In order to provide a further comparison, the axial-force and resultant-force coefficients were computed by using inviscid Newtonian theory. These values are also shown in figure 13.

The base-drag coefficients were obtained by using data from reference 10 and by assuming that the variation of base drag with angle of incidence was negligibly small for these tests. The base-pressure coefficients were added to the total forebody axial-force coefficients (fig. 13(a)) and the results are plotted in figure 12. In order to obtain comparable data for the Newtonian estimate, skin-friction-drag coefficients were calculated for laminar and turbulent boundary layers and added to the total forebody axial-force coefficients. These calculations were made with the use of the flight-test Mach numbers and Reynolds numbers, and the shaded region of figure 12 shows the results.

In addition to resultant-force coefficients obtained by the two aforementioned methods, estimates were made at lower Mach numbers by superimposing a cross-flow increment (ref. 18) on the inviscid flow, as proposed in reference 19. These estimates are plotted in figure 13(b).

REFERENCES

1. Foster, Gerald V.: Static Stability Characteristics of a Series of Hypersonic Boost-Glide Configurations at Mach Numbers of 1.41 and 2.01. NASA TM X-167, 1959.
2. Hoffman, Sherwood; and Blanchard, Willard S., Jr.: Free-Flight Investigation at Supersonic Speeds of the Stability and Drag of a 79° Clipped Delta Boost-Glide Configuration Including an Analog Study of Coupled Motions During the Flight. NASA TM X-425, 1961.
3. Judd, Joseph H.; and Woodbury, Gerard E.: Free-Flight Tests to a Mach Number of 1.5 of Slender Triangular Pyramid Reentry Configurations. NASA TM X-437, 1961.
4. Minzner, R. A.; Ripley, W. S.; and Condron, T. P.: U.S. Extension to the ICAO Standard Atmosphere – Tables and Data to 300 Standard Geopotential Kilometers. Geophys. Res. Directorate and U.S. Weather Bureau, 1958.
5. Gillis, Clarence L.; and Mitchell, Jesse L.: Determination of Longitudinal Stability and Control Characteristics From Free-Flight Model Tests With Results at Transonic Speeds for Three Airplane Configurations. NACA Rept. 1337, 1957.
6. Nelson, Robert L.: The Motions of Rolling Symmetrical Missiles Referred to a Body-Axis System. NACA TN 3737, 1956.
7. Van Driest, E. R.: Turbulent Boundary Layer on a Cone in a Supersonic Flow at Zero Angle of Attack. J. Aeron. Sci., vol. 19, no. 1, Jan. 1952, pp. 55-57, 72.
8. Van Driest, E. R.: Turbulent Boundary Layer in Compressible Fluids. J. Aeron. Sci., vol. 18, no. 3, Mar. 1951, pp. 145-160, 216.
9. Hayes, Wallace D.; and Probstein, Ronald F.: Viscous Hypersonic Similitude. J. Aero/Space Sci., vol. 26, no. 12, Dec. 1959, pp. 815-824.
10. Love, Eugene S.: Base Pressure at Supersonic Speeds on Two-Dimensional Airfoils and on Bodies of Revolution With and Without Fins Having Turbulent Boundary Layers. NACA TN 3819, 1957. (Supersedes NACA RM L53C02.)
11. Price, D. A., Jr.; and Nelson, E. O.: The Aerobee 150A Roll Lock-In Study. Contract No. NAS 5-9061, Lockheed Missiles and Space Co., [1965].
12. Pettus, Joseph J.: Persistent Re-Entry Vehicle Roll Resonance. AIAA Paper No. 66-49, Jan. 1966.
13. Van Dyke, Milton D.: The Combined Supersonic-Hypersonic Similarity Rule. J. Aeron. Sci. (Readers' Forum), vol. 18, no. 7, July 1951, pp. 499-500.
14. Jorgensen, Leland H.: Elliptic Cones Alone and With Wings at Supersonic Speeds. NACA TN 4045, 1957.

15. Shantz, I.: Cone Static Stability Investigation at Mach Numbers 1.56 Through 4.24. NAVORD Rept. 3584, U.S. Naval Ord. Lab. (White Oak, Md.), Dec. 7, 1953. (Available as ASTIA Doc. AD 128203.)
16. Dennis, David H.; and Cunningham, Bernard E.: Forces and Moments on Pointed and Blunt-Nosed Bodies of Revolution at Mach Numbers From 2.75 to 5.00. NACA RM A52E22, 1952.
17. Penland, Jim A.: Aerodynamic Force Characteristics of a Series of Lifting Cone and Cone-Cylinder Configurations at a Mach Number of 6.83 and Angles of Attack Up to 130° . NASA TN D-840, 1961.
18. Schwabe, M.: Pressure Distribution in Nonuniform Two-Dimensional Flow. NACA TM 1039, 1943.
19. Kelly, Howard R.: The Estimation of Normal-Force, Drag, and Pitching-Moment Coefficients for Blunt-Based Bodies of Revolution at Large Angles of Attack. J. Aeron. Sci., vol. 21, no. 8, Aug. 1954, pp. 549-555, 565.

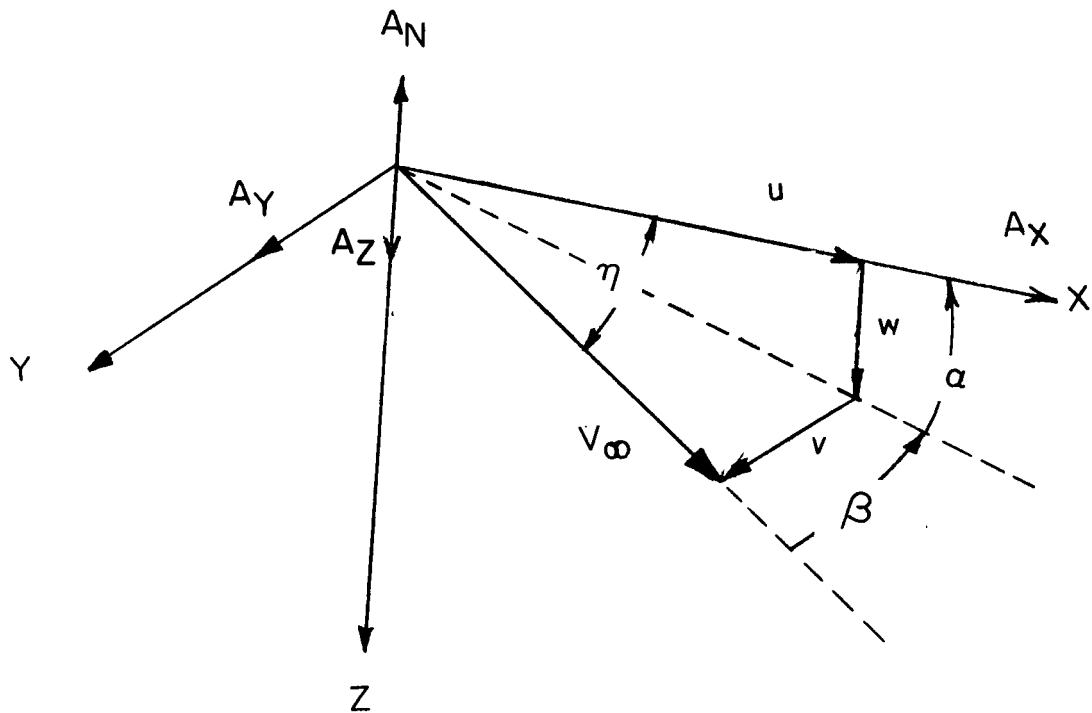
TABLE I.- GEOMETRIC AND MASS CHARACTERISTICS OF FLIGHT-TEST MODEL

Base area (reference area), ft ² (m ²)	0.545 (0.0506)
Planform area, ft ² (m ²)	2.776 (0.258)
Surface area, ft ² (m ²)	8.795 (0.817)
Diameter (reference length), ft (m)	0.833 (0.254)
Model total weight, lbf (N)	113.500 (505)
Longitudinal location of center of gravity measured	
from reference station 0, ft (m)	4.033 (1.229)
Moment of inertia about X-axis, slug-ft ² (kg-m ²)	0.230 (0.312)
Moment of inertia about Y-axis, slug-ft ² (kg-m ²)	9.666 (13.10)
Moment of inertia about Z-axis, slug-ft ² (kg-m ²)	9.666 (13.10)

TABLE II.- LINEAR-ACCELEROMETER LOCATIONS

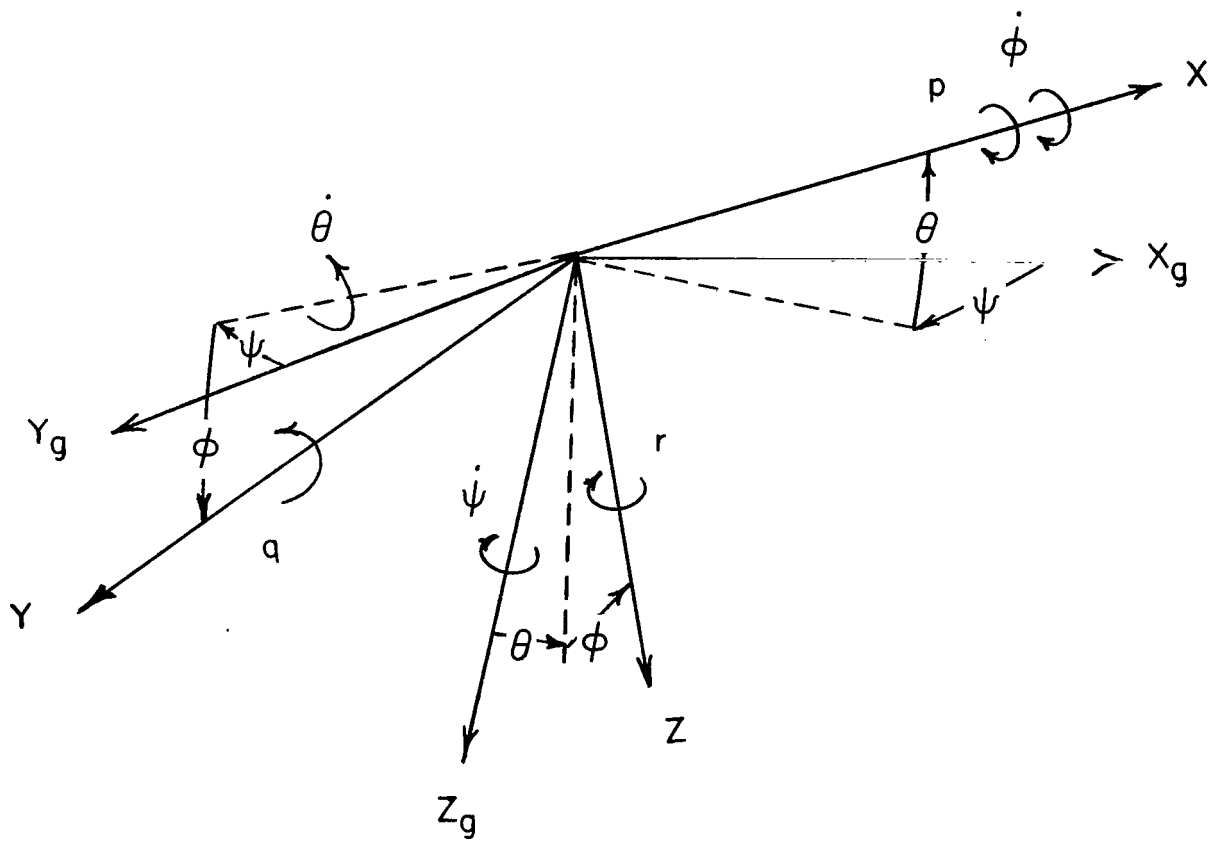
[Dimensions, given first in inches and parenthetically in meters, are with respect to the model center of gravity]

Instrument	x	y	z
Transverse accelerometer:			
Forward instrument	-2.510 (-0.064)	0	0
Rearward instrument	-18.650 (-0.474)	0	0
Normal accelerometer:			
Forward instrument	-1.200 (-0.030)	0	0
Rearward instrument	-16.780 (-0.426)	0	0
Longitudinal accelerometer:			
High-range instrument	-0.146 (-0.004)	0.500 (0.013)	0
Low-range instrument	-0.146 (-0.004)	-0.500 (-0.013)	0



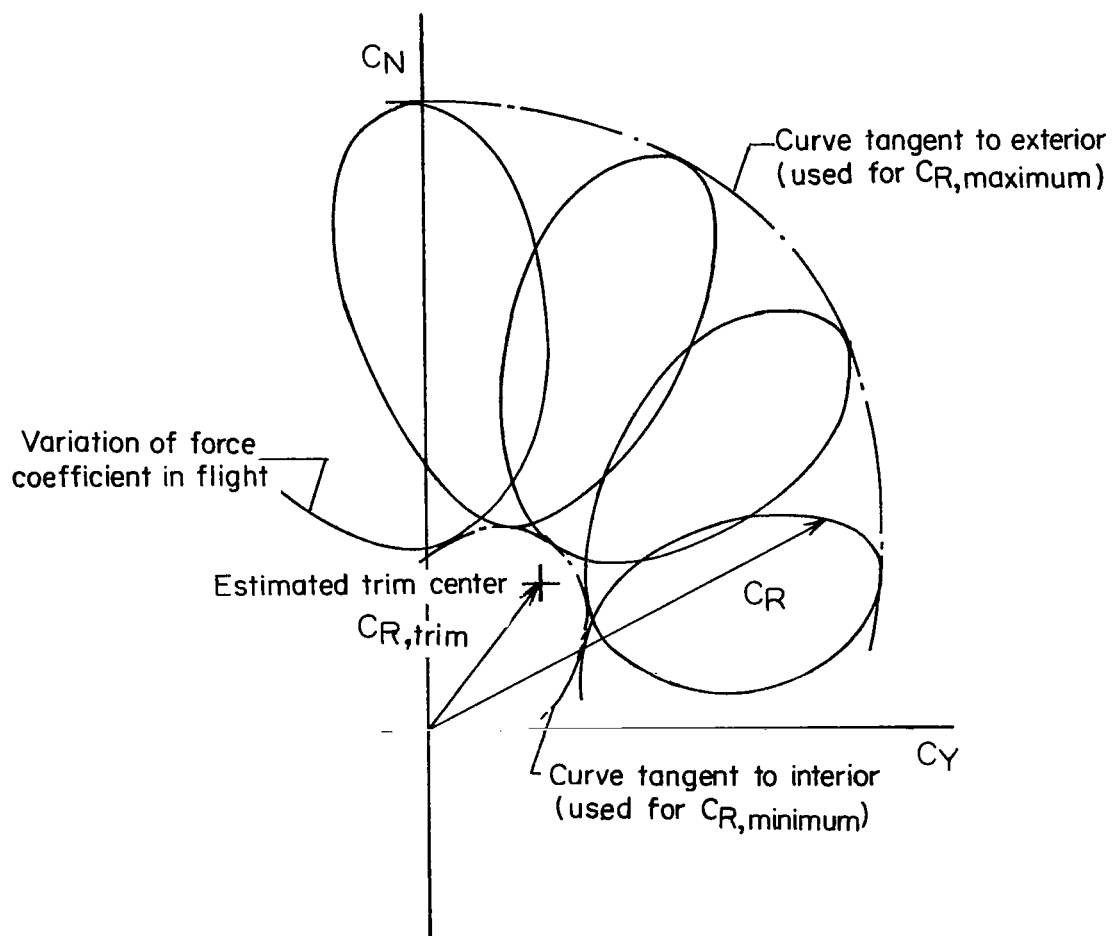
(a) Relative velocities and angular orientation of the mean velocity vector with respect to the body-axis system.

Figure 1.- Geometric relationships of force coefficients and various axis systems.



(b) Gravity-axis and body-axis systems.

Figure 1.- Continued.



(c) Force coefficients.

Figure 1.- Concluded.

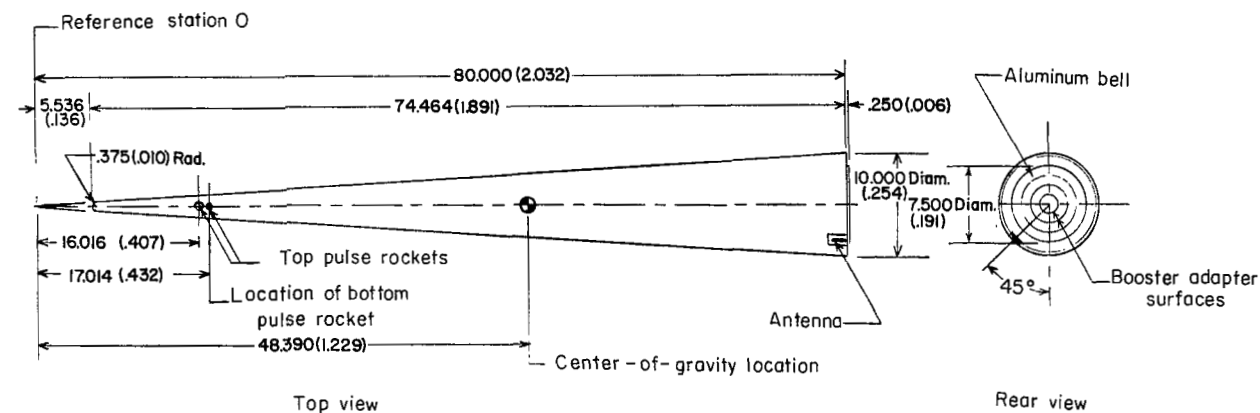
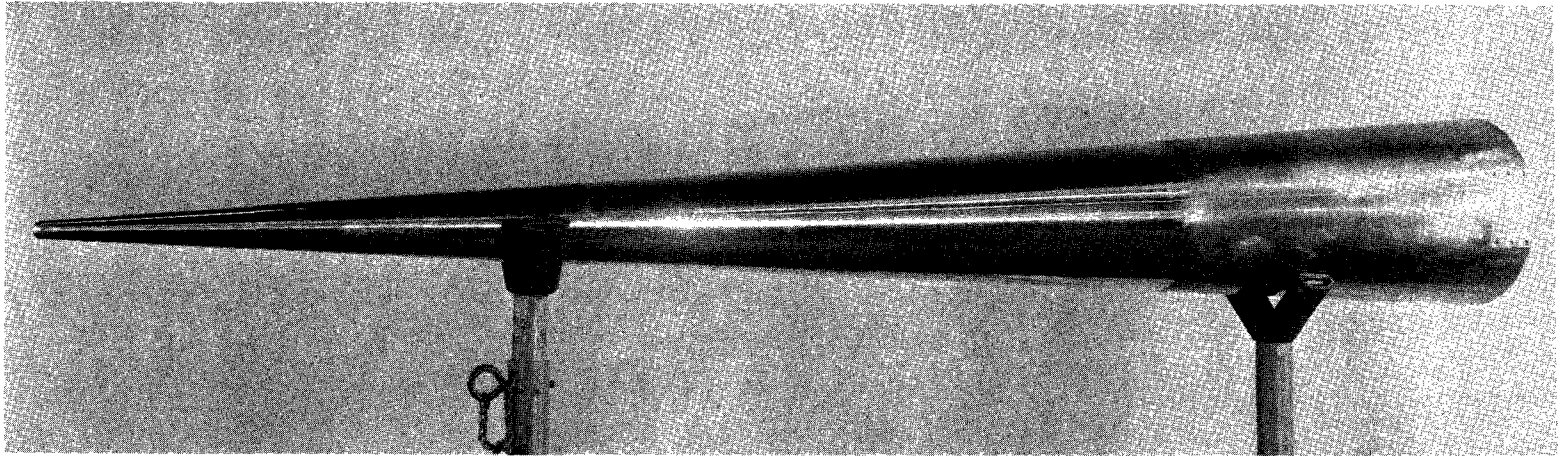
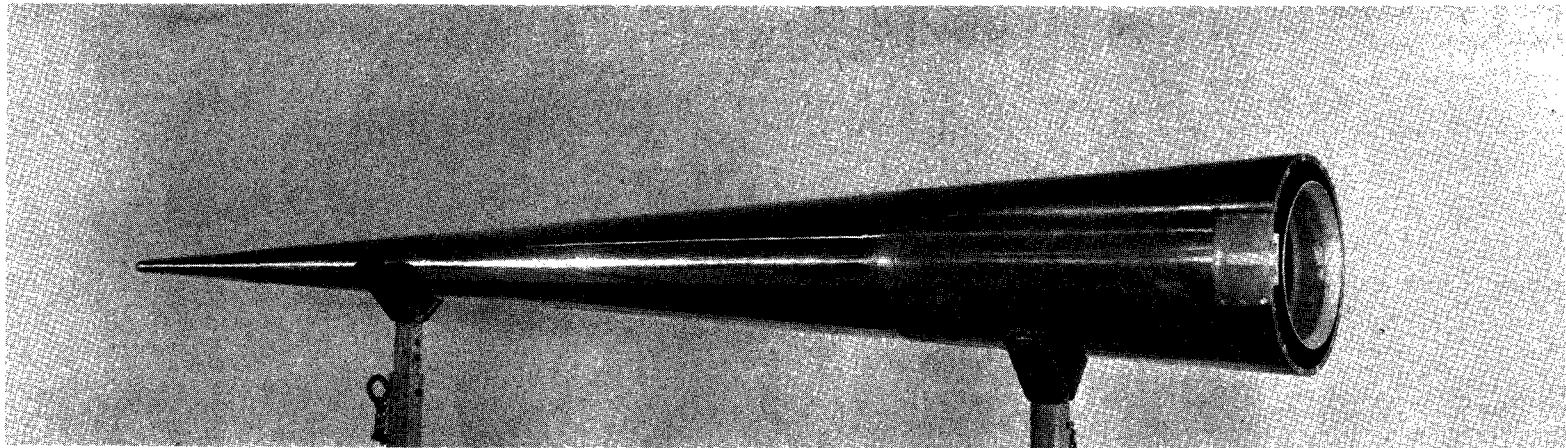


Figure 2.- Drawing of flight-test configuration. (Dimensions are given first in inches and parenthetically in meters.)



(a) Top front view.

L-60-4625



(b) Top rear view.

L-60-4626

Figure 3.- Photographs of flight-test model.

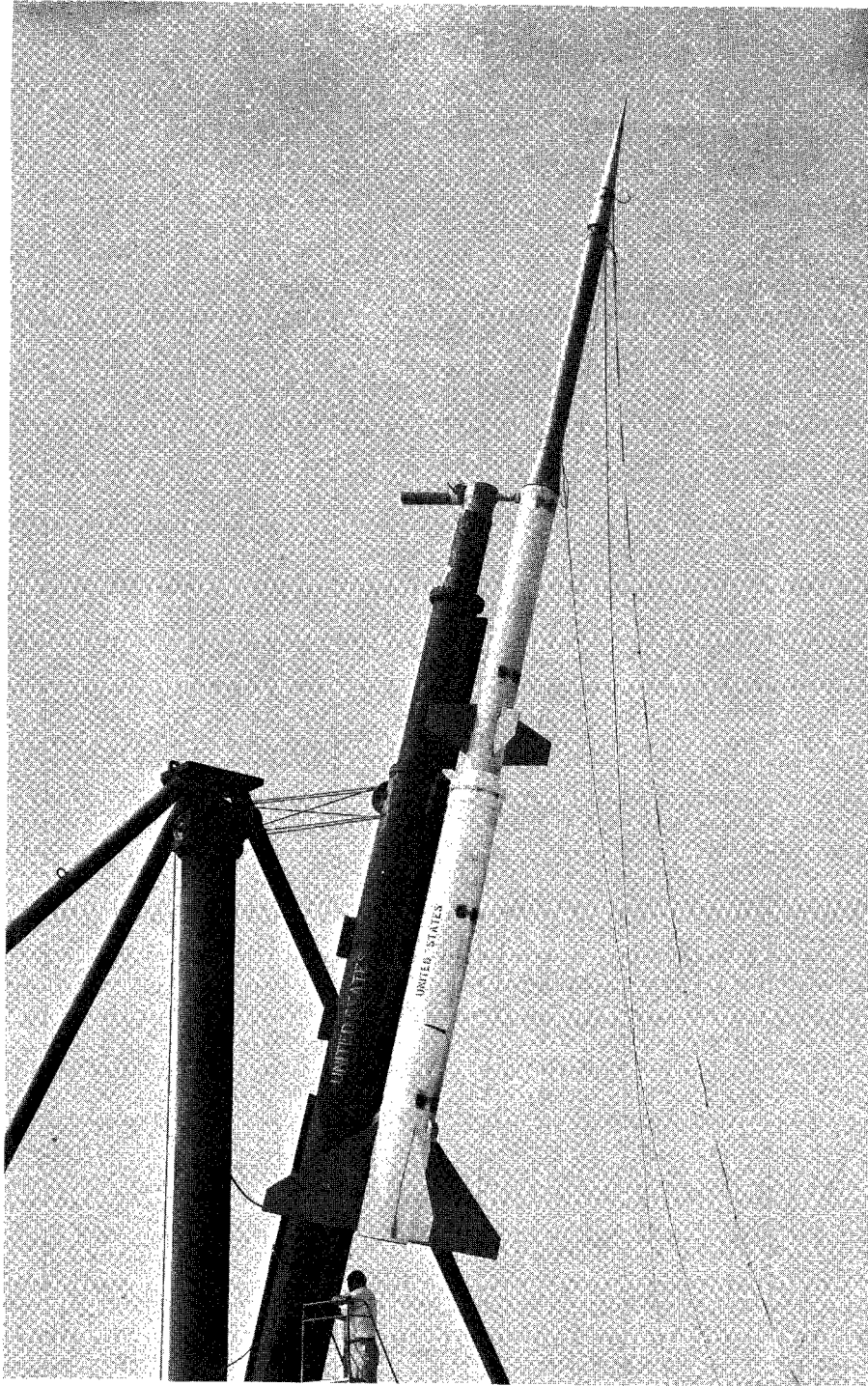


Figure 4.- Assembled vehicle mounted on launcher.

L-60-5157

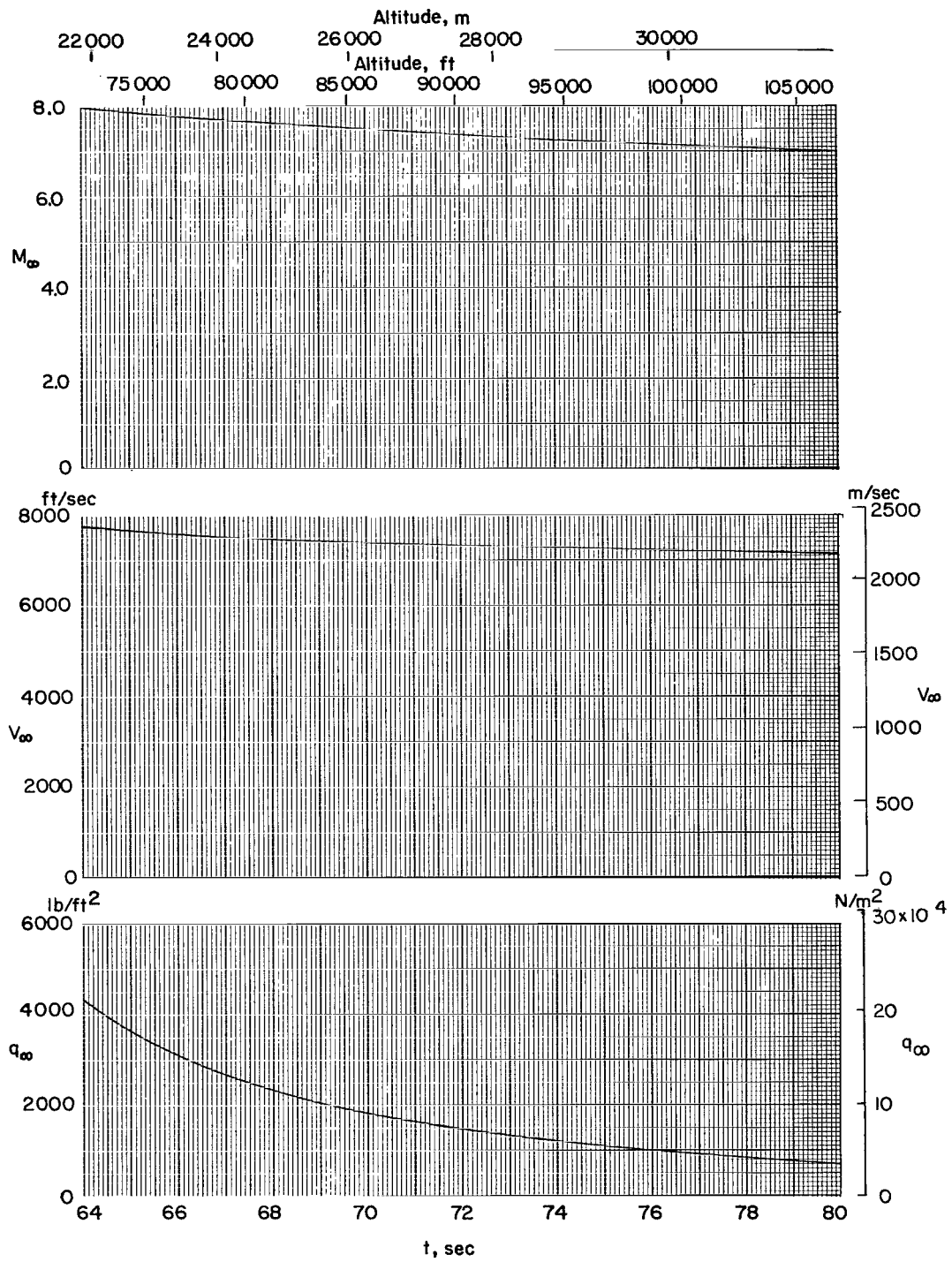


Figure 5.- Test conditions during decelerating flight.

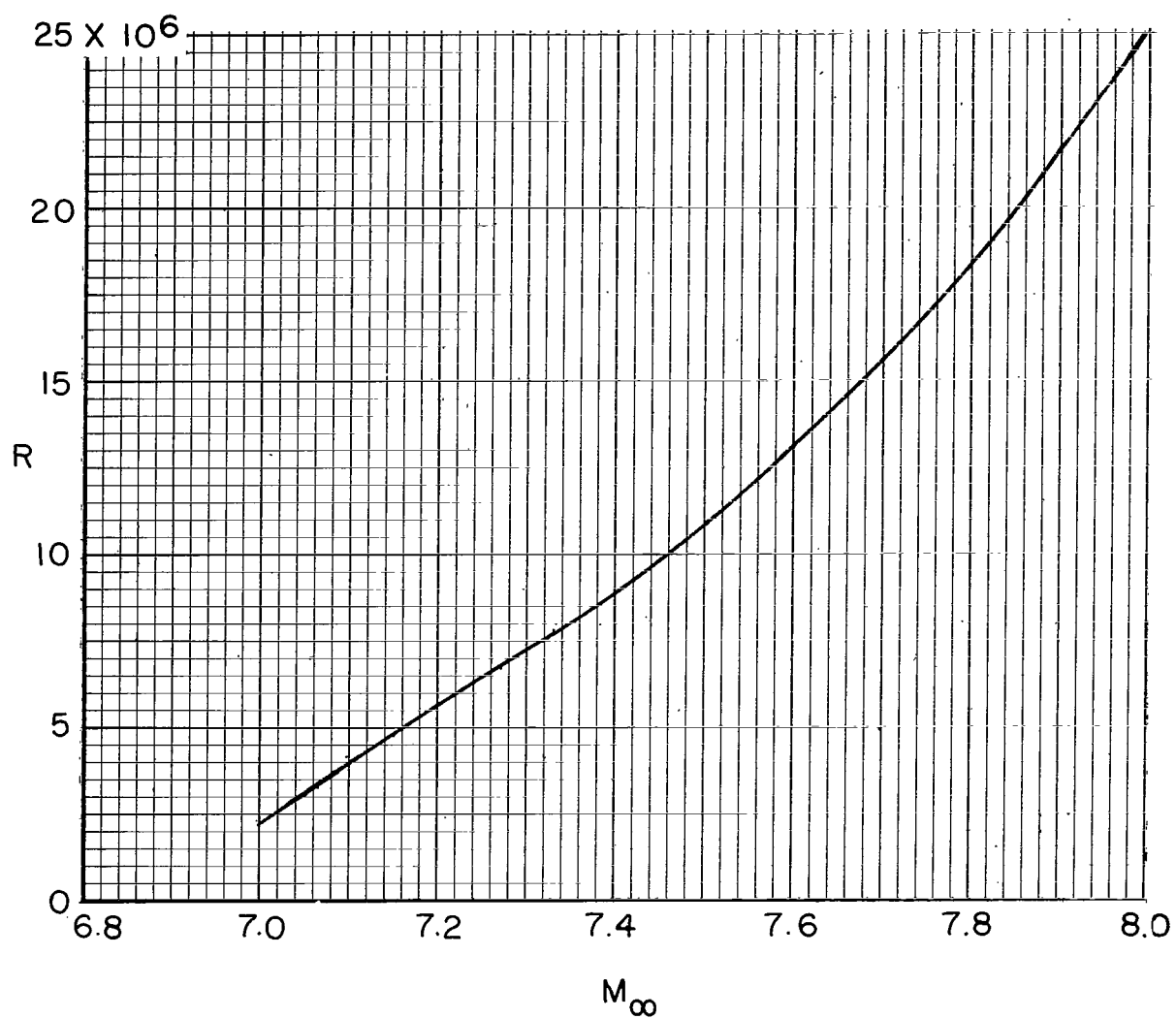
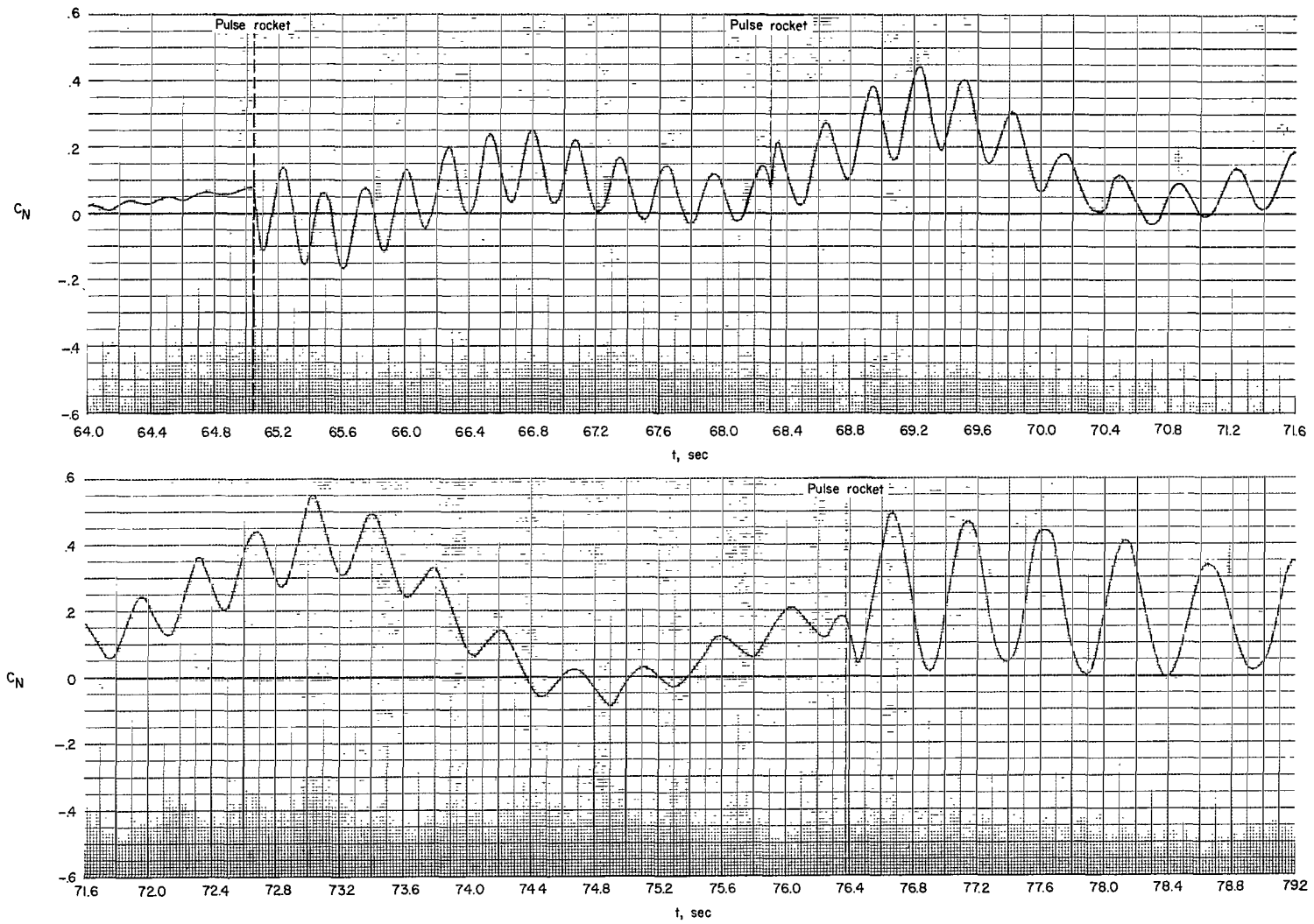
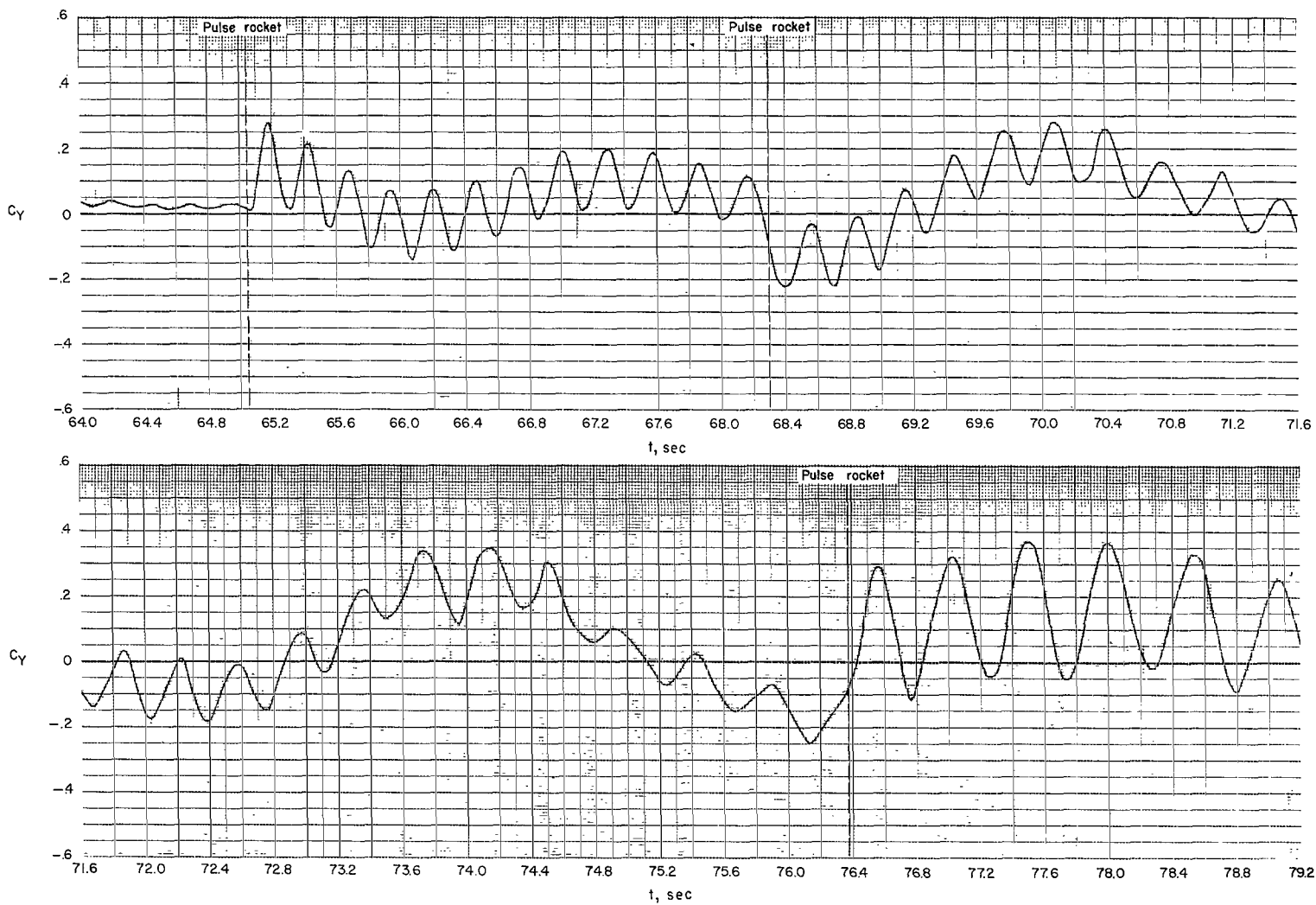


Figure 6.- Variation of Reynolds number based on body length with Mach number for the flight-test model.



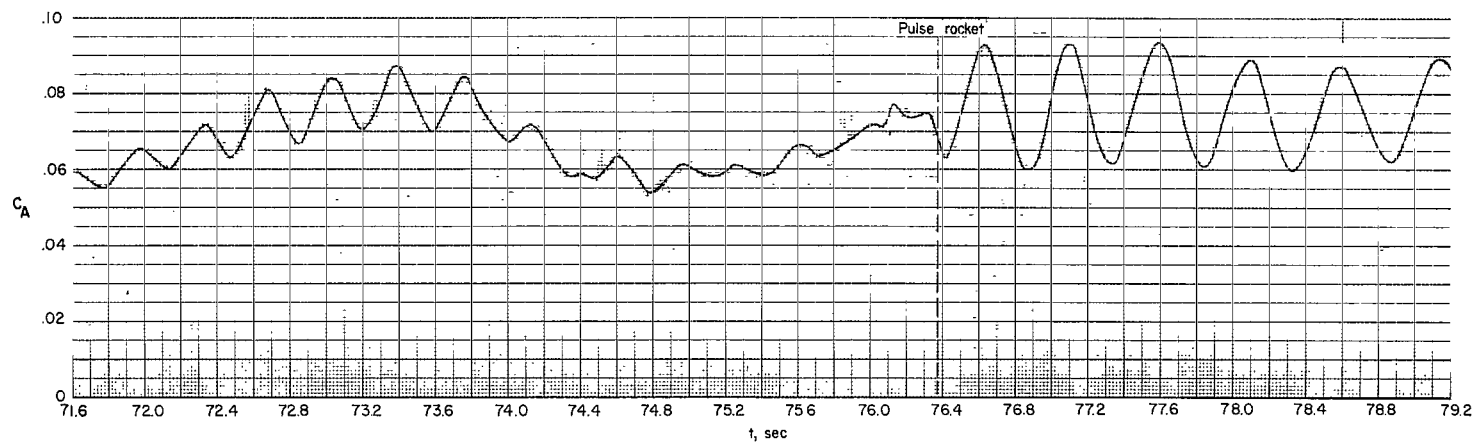
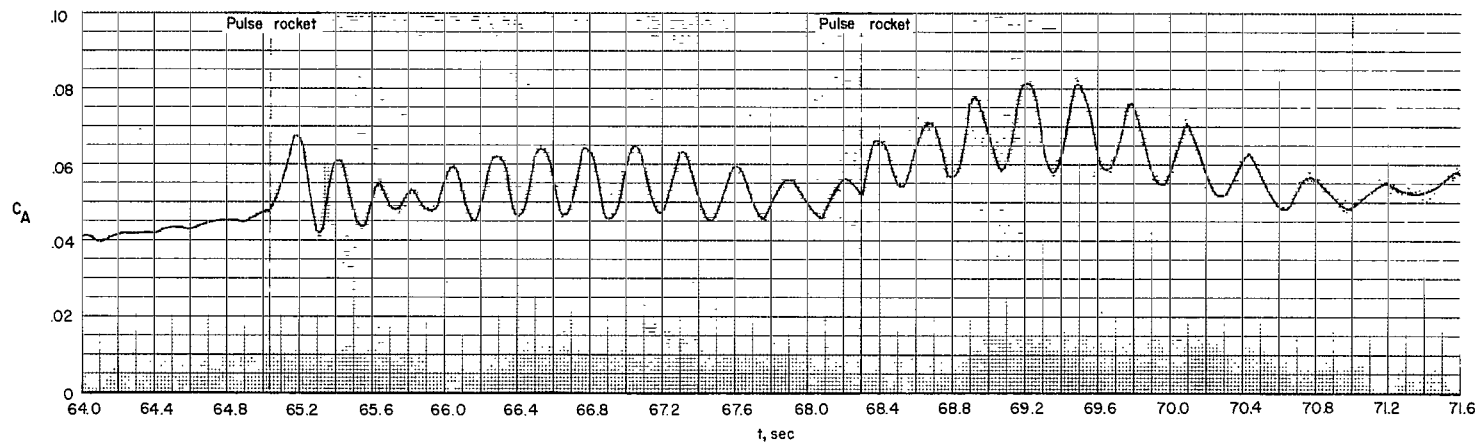
(a) Variation of normal-force coefficient with time.

Figure 7.- Measured aerodynamic coefficients of cone.



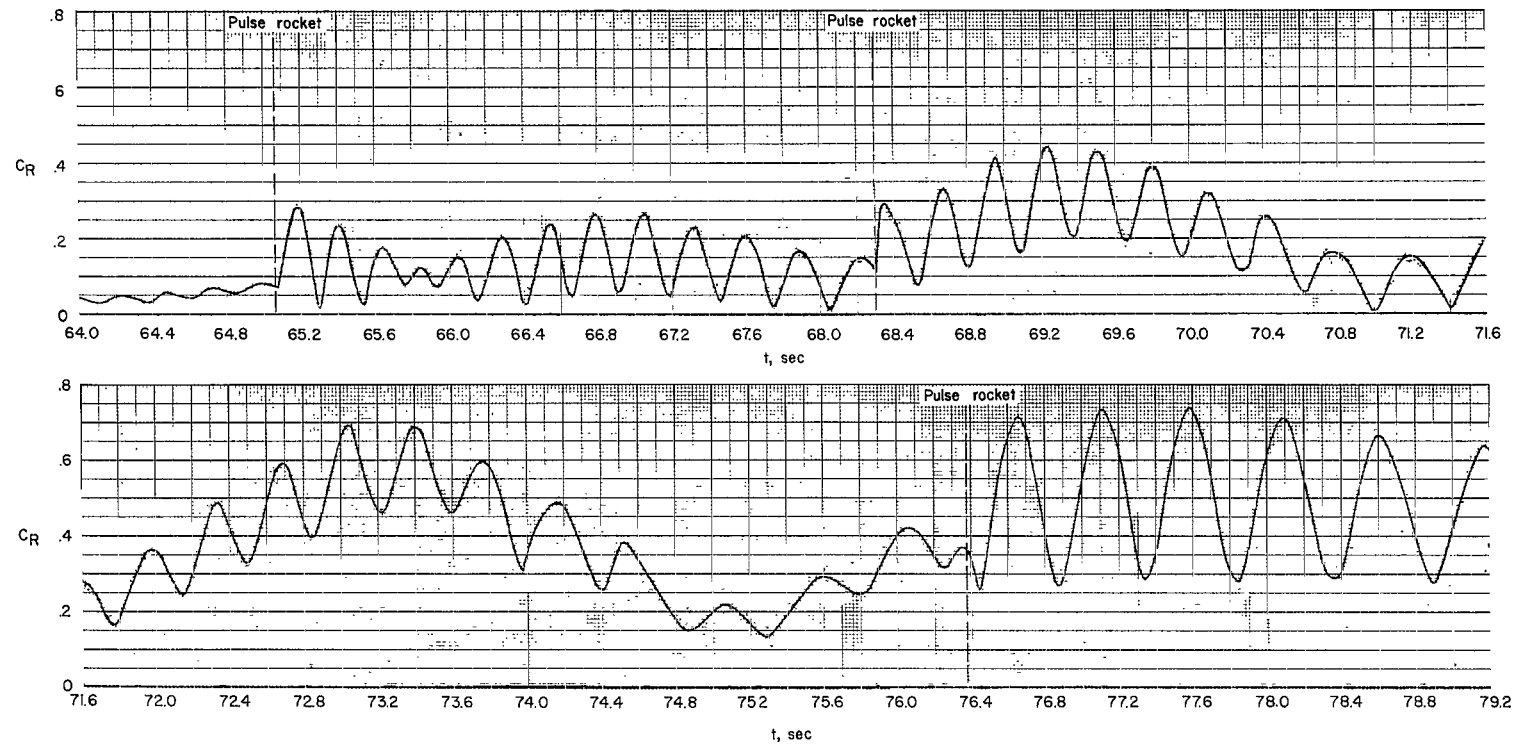
(b) Variation of side-force coefficient with time.

Figure 7.- Continued.



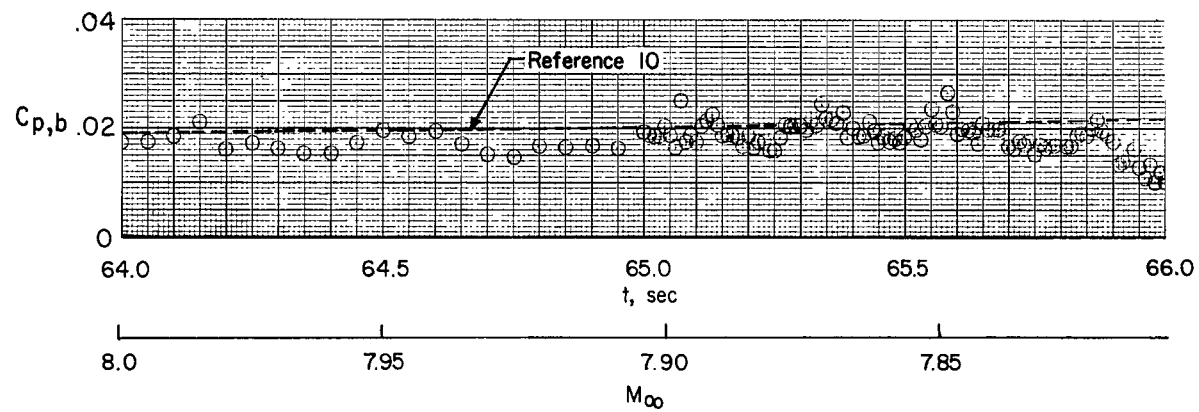
(c) Variation of axial-force coefficient with time.

Figure 7.- Continued.



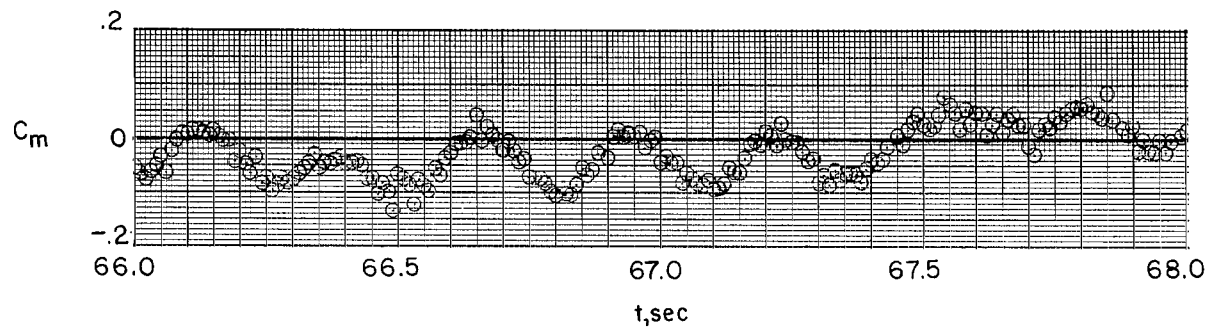
(d) Variation of resultant-force coefficient with time.

Figure 7.- Continued.

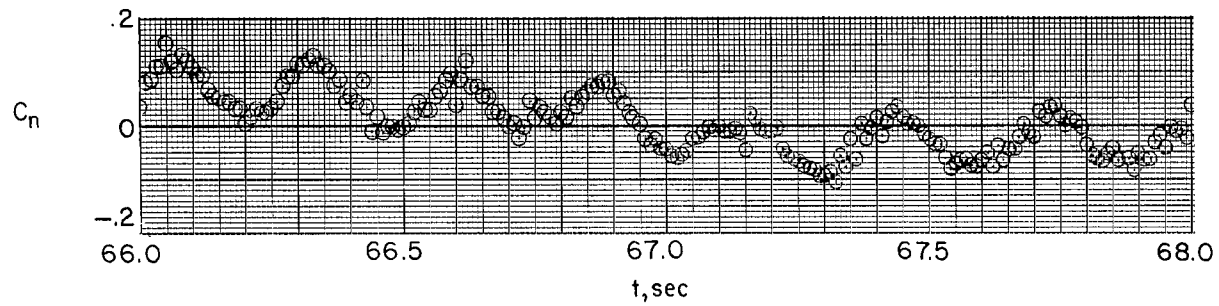


(e) Variation of base-pressure coefficient with time.

Figure 7.- Continued.



(f) Variation of total pitching-moment coefficient with time.



(g) Variation of total yawing-moment coefficient with time.

Figure 7.- Concluded.

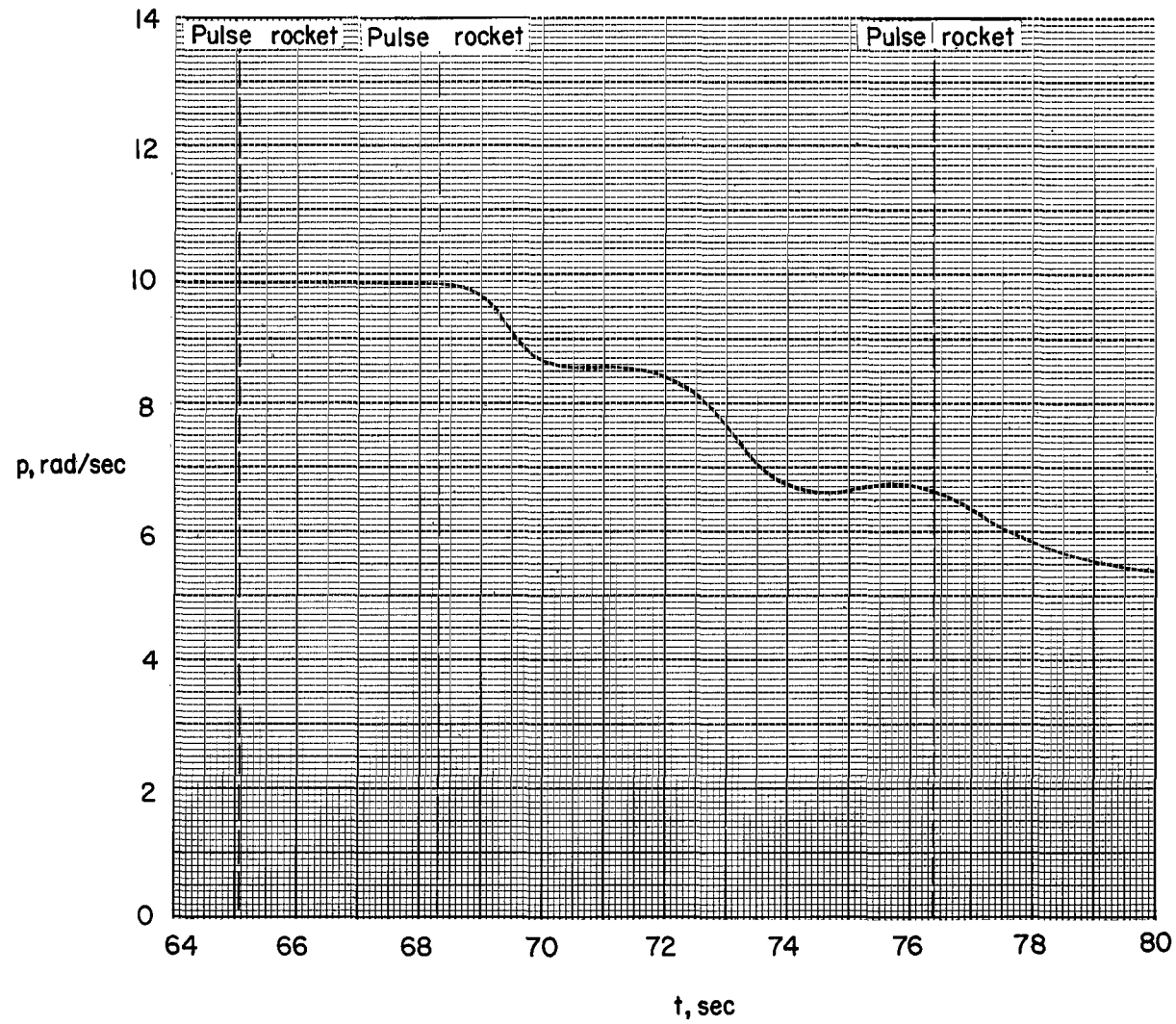
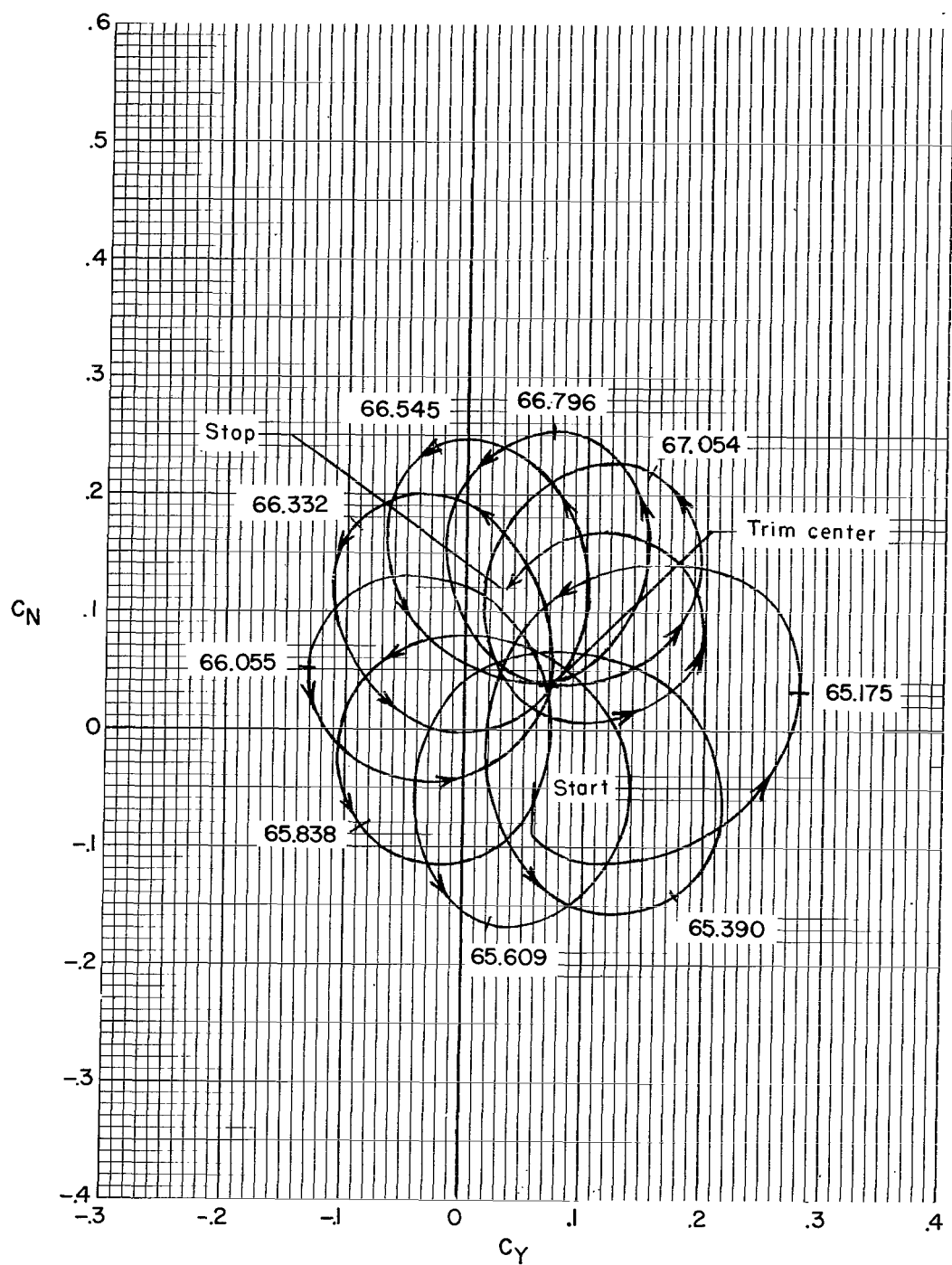
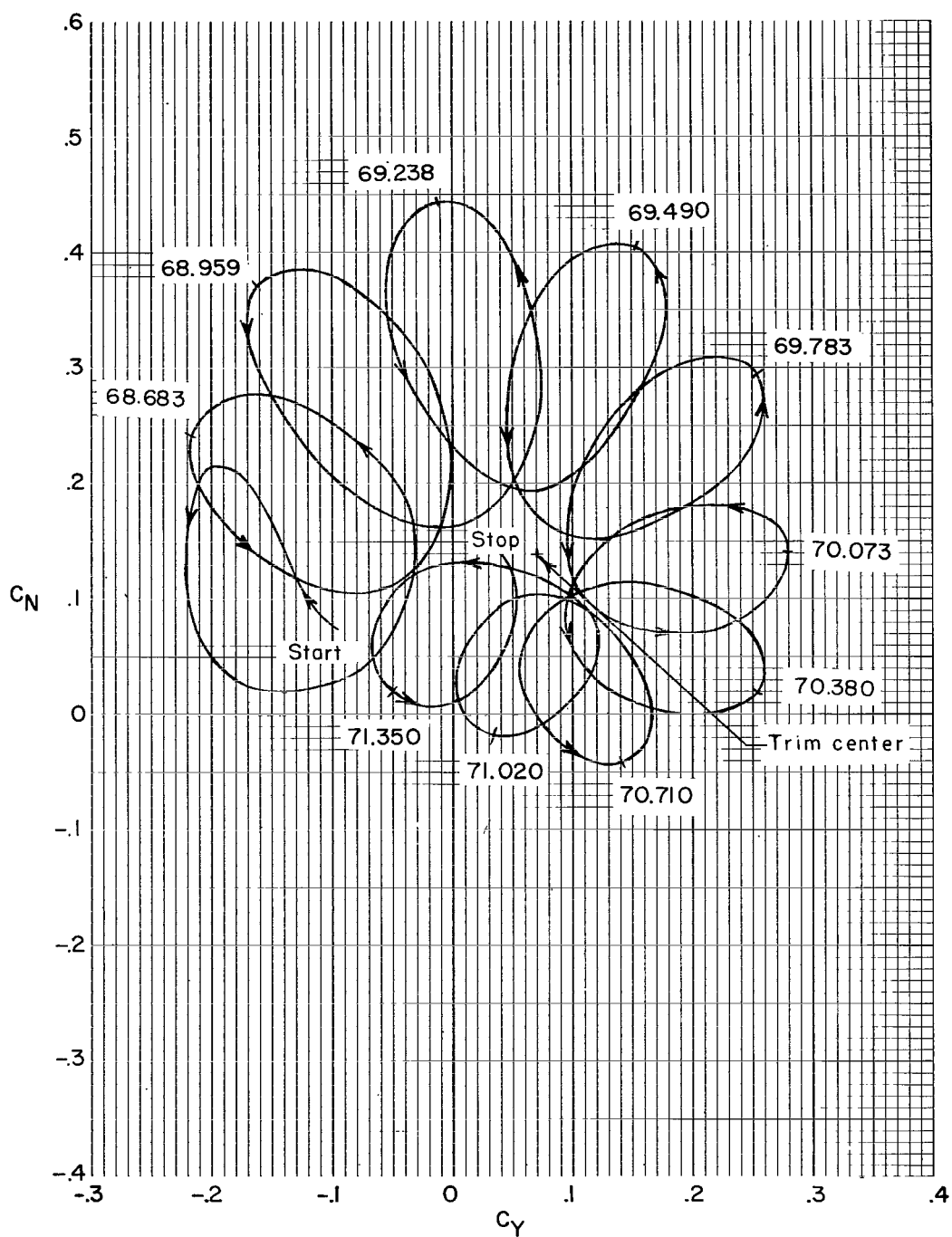


Figure 8.- Variation of the cone roll velocity with time.



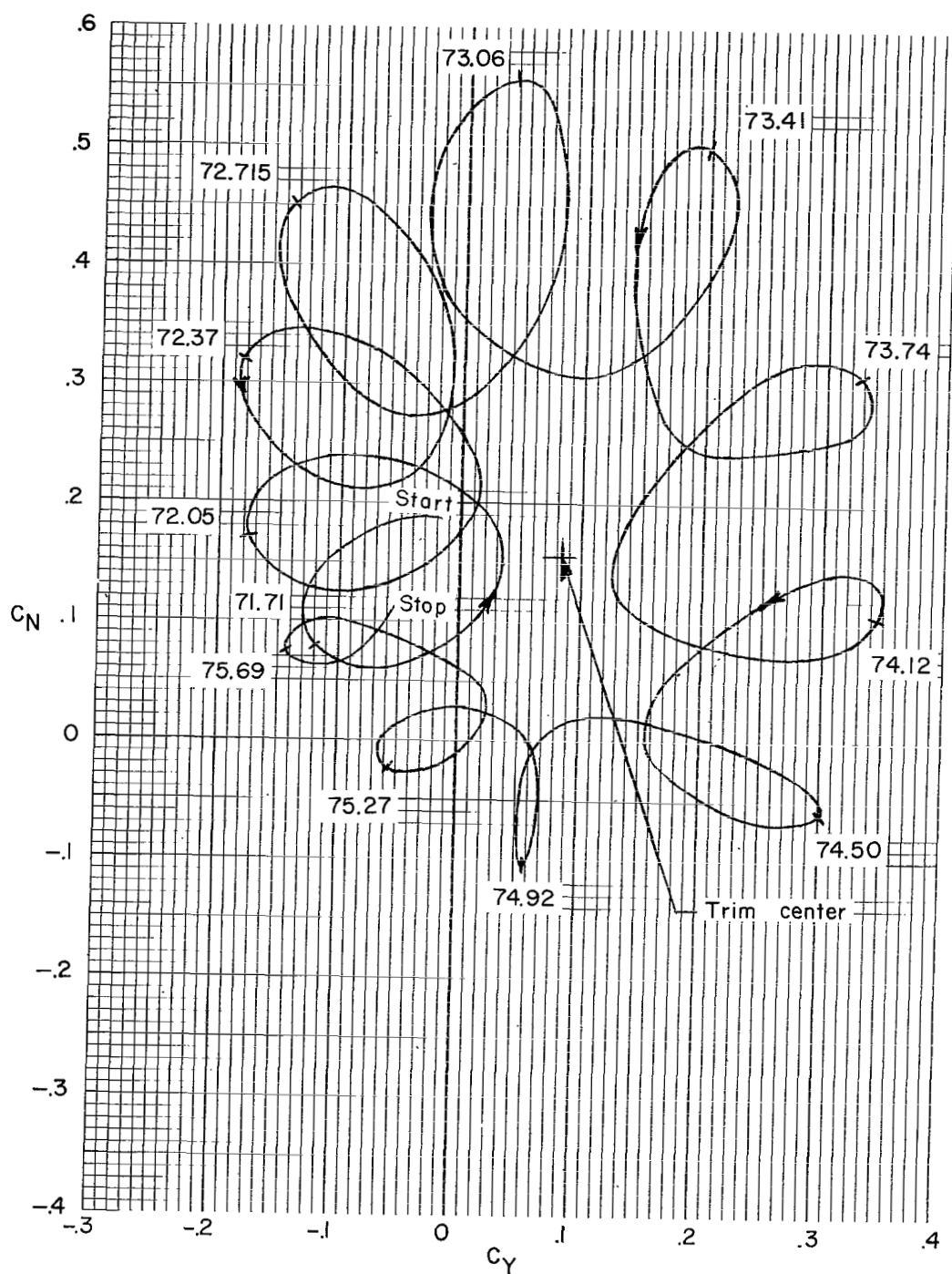
(a) Cycles from 65.0 to 67.1 seconds.

Figure 9.- Model force-coefficient relationships.



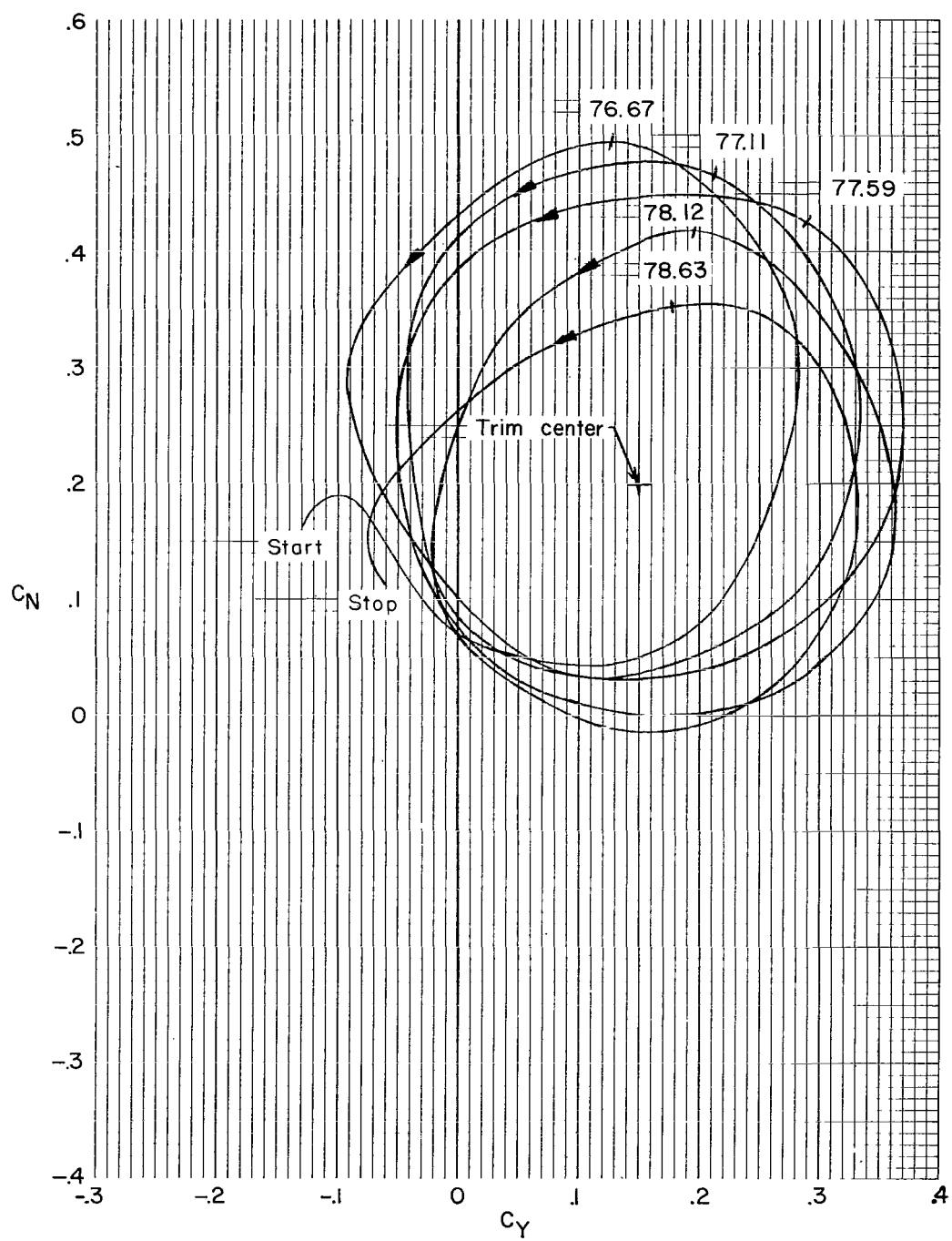
(b) Cycles from 68.3 to 71.4 seconds.

Figure 9.- Continued.



(c) Cycles from 71.5 to 75.9 seconds.

Figure 9.- Continued.



(d) Cycles from 76.3 to 78.8 seconds.

Figure 9.- Concluded.

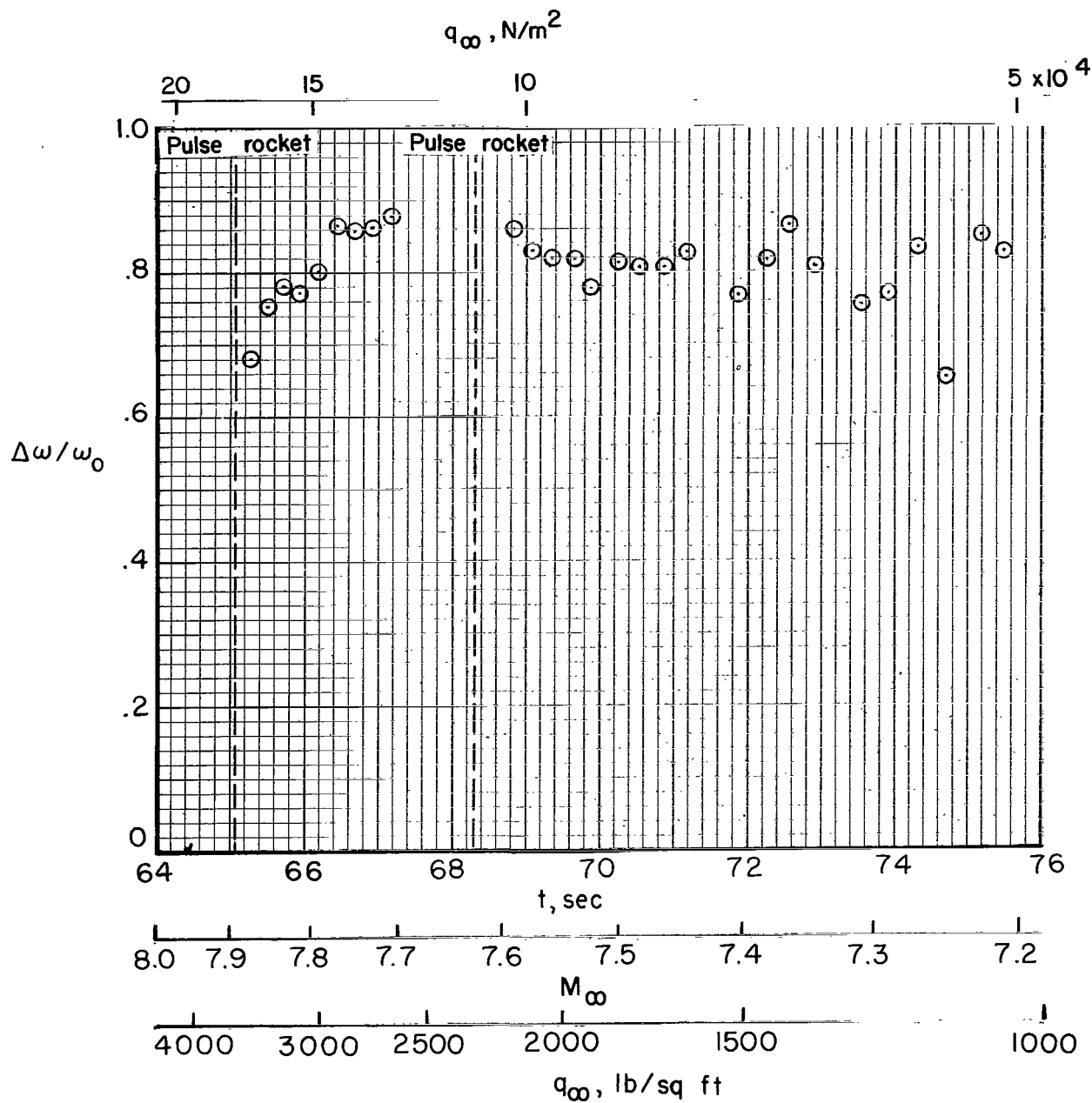


Figure 10.- Variation of roll resonance parameter with time.

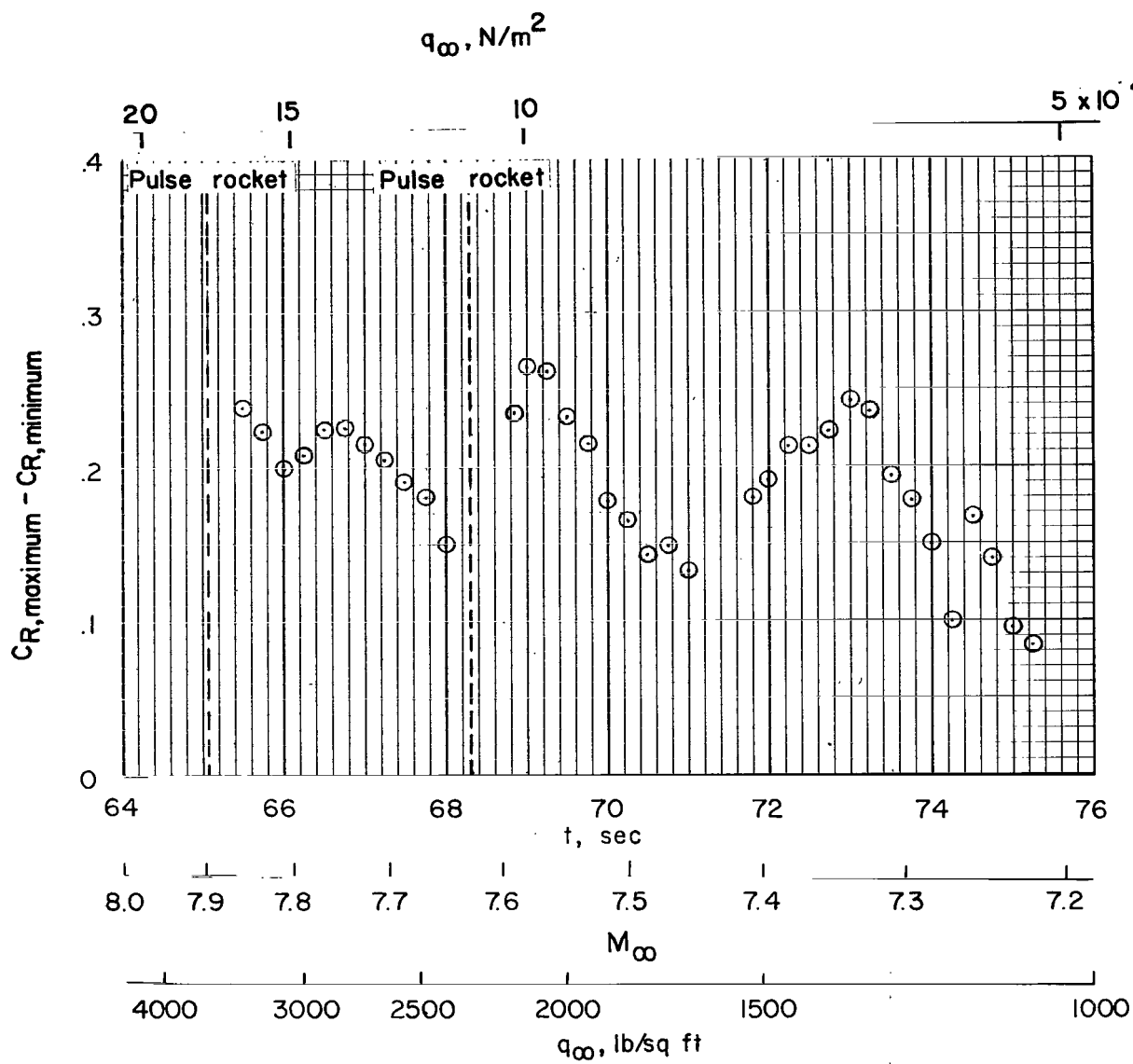


Figure 11.- Variation of resultant-force amplitude with time.

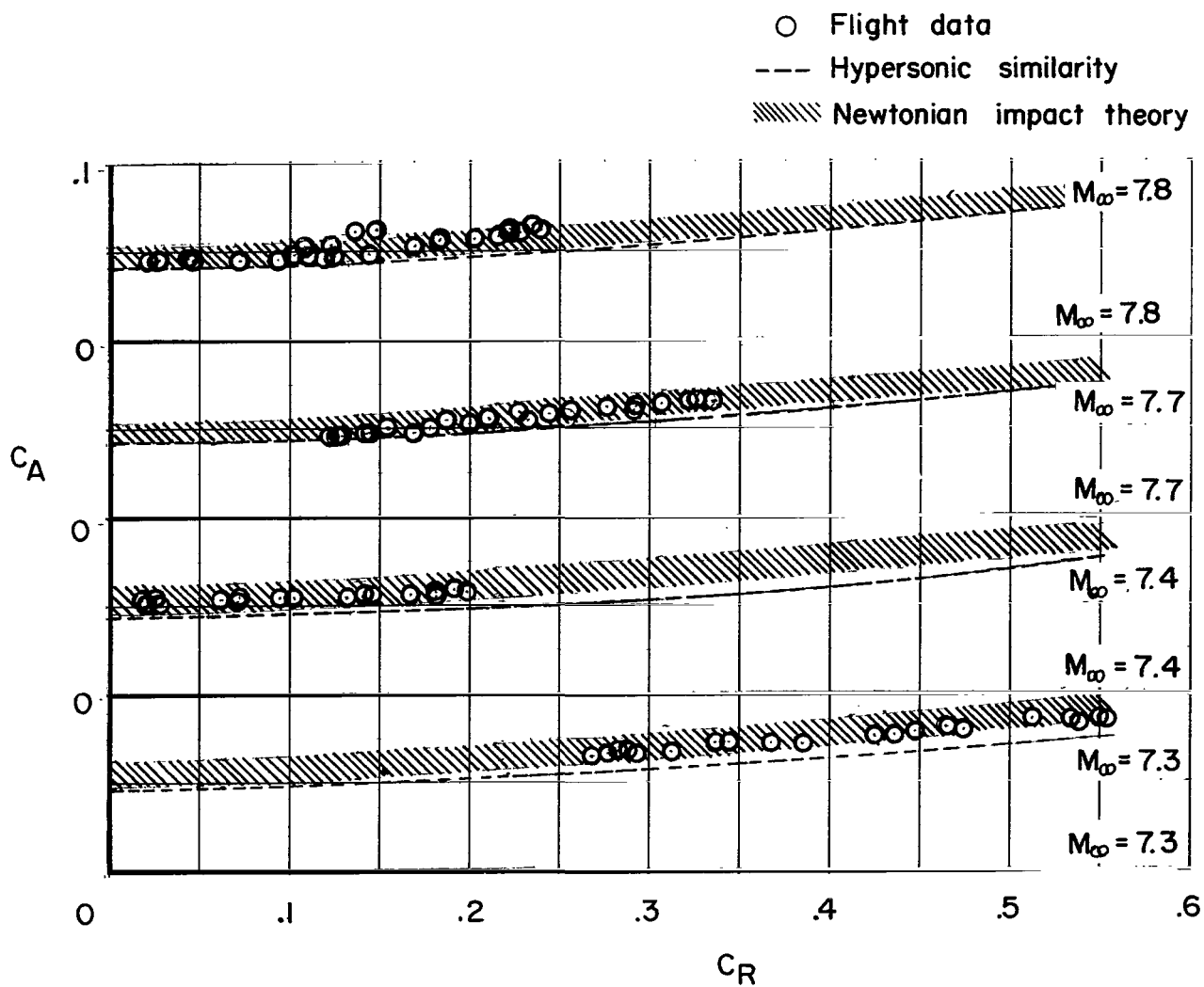
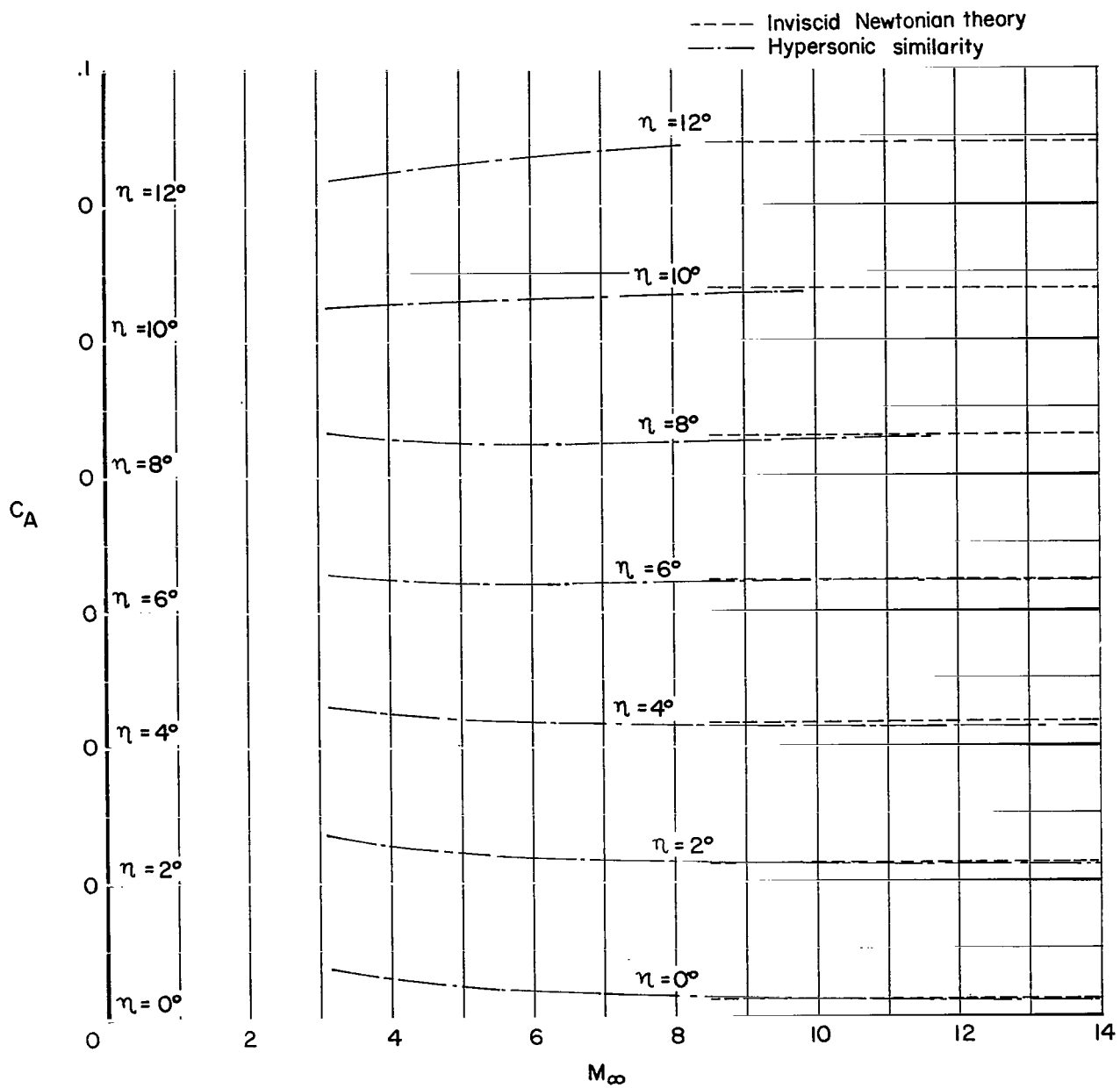
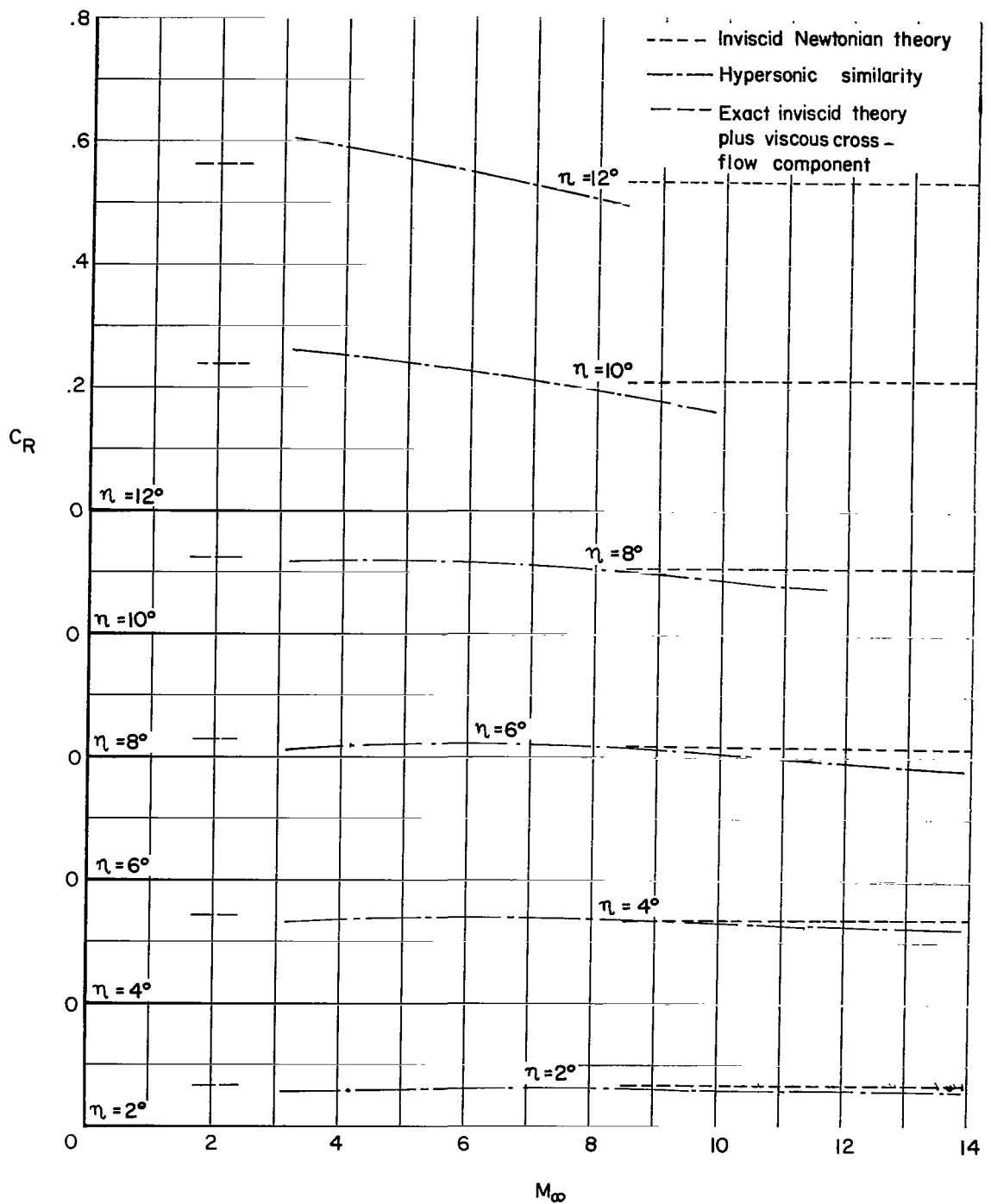


Figure 12.- Variation of axial-force coefficient with resultant-force coefficient at several Mach numbers.



(a) Axial-force coefficients.

Figure 13.- Estimated variation of cone force coefficients with Mach number for several angles of incidence.



(b) Resultant-force coefficients.

Figure 13.- Concluded.

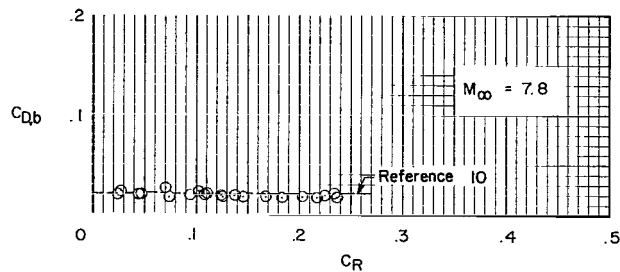
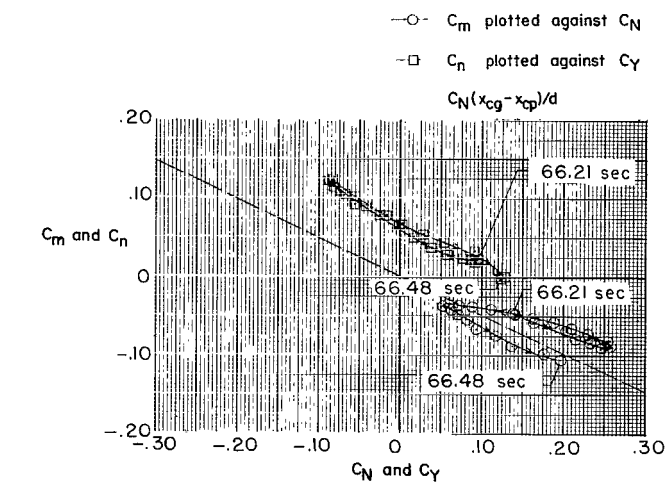
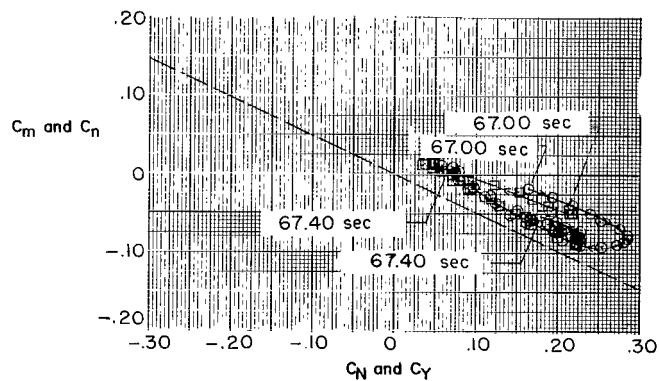


Figure 14.- Variation of base-drag coefficient with resultant-force coefficient at a free-stream Mach number of 7.8.



(a) $M_{\infty} \approx 7.78$.



(b) $M_{\infty} \approx 7.70$.

Figure 15.- Variation of moment coefficients with force coefficients at two Mach numbers.

"The aeronautical and space activities of the United States shall be conducted so as to contribute . . . to the expansion of human knowledge of phenomena in the atmosphere and space. The Administration shall provide for the widest practicable and appropriate dissemination of information concerning its activities and the results thereof."

—NATIONAL AERONAUTICS AND SPACE ACT OF 1958

NASA SCIENTIFIC AND TECHNICAL PUBLICATIONS

TECHNICAL REPORTS: Scientific and technical information considered important, complete, and a lasting contribution to existing knowledge.

TECHNICAL NOTES: Information less broad in scope but nevertheless of importance as a contribution to existing knowledge.

TECHNICAL MEMORANDUMS: Information receiving limited distribution because of preliminary data, security classification, or other reasons.

CONTRACTOR REPORTS: Scientific and technical information generated under a NASA contract or grant and considered an important contribution to existing knowledge.

TECHNICAL TRANSLATIONS: Information published in a foreign language considered to merit NASA distribution in English.

SPECIAL PUBLICATIONS: Information derived from or of value to NASA activities. Publications include conference proceedings, monographs, data compilations, handbooks, sourcebooks, and special bibliographies.

TECHNOLOGY UTILIZATION PUBLICATIONS: Information on technology used by NASA that may be of particular interest in commercial and other non-aerospace applications. Publications include Tech Briefs, Technology Utilization Reports and Notes, and Technology Surveys.

Details on the availability of these publications may be obtained from:

SCIENTIFIC AND TECHNICAL INFORMATION DIVISION
NATIONAL AERONAUTICS AND SPACE ADMINISTRATION

Washington, D.C. 20546